Spring 2015

Experimental and computational evaluation of water management and performance of a bio-inspired PEM fuel cell in comparison to a conventional flow field

Venkatanaga Bhaskar Prakash Saripella

Department:

EXPERIMENTAL AND COMPUTATIONAL EVALUATION OF WATER MANAGEMENT AND PERFORMANCE OF A BIO-INSPIRED PEM FUEL CELL IN COMPARISON TO A CONVENTIONAL FLOW FIELD

by

VENKATANAGA BHASKAR PRAKASH SARIPELLA

A THESIS

Presented to the Faculty of the Graduate School of the

MISSOURI UNIVERSITY OF SCIENCE AND TECHNOLOGY

In Partial Fulfillment of the Requirements for the Degree

MASTER OF SCIENCE IN MECHANICAL ENGINEERING

2015

Approved by

Dr. Umit Koylu, Advisor
Dr. Ming C. Leu Co-Advisor
Dr. Kakkattukuzhy M. Isaac

ABSTRACT

Fuel cells are being increasingly used in various stationary and transportation power applications due to their higher energy efficiency and lower pollution. Flow field design in Proton Exchange Membrane (PEM) fuel cells is a major area of research for performance improvement. Bio-inspired flow field designs have significant potential for increased performance by effective distribution of reactants with better water management capabilities. In this study, a bio-inspired flow field design, formulated using Murray's law and mimicking a typical leaf venation pattern, is experimentally and computationally investigated in comparison to a conventional single serpentine design. Experiments are conducted using a special transparent fuel cell assembly with copper as the conductive channel and current collector so that liquid water within the fuel cell channels can be directly visualized. Overall performances of both bio-inspired and conventional PEM fuel cells are also quantified with the corresponding polarization and power curves. Moreover, advanced computational simulations are carried out to predict pressure, velocity, and reactant and product distributions within the cells. The measurements and simulations clearly demonstrate the superior performance of the bio-inspired design with a 30% increase in peak power density in comparison to the conventional design. The observed water management capabilities as well as the computed parameters support and complement this overall result, quantify different types of two-phase flows within the fuel cell micro-channels, and help elucidate the underlying physical and electrochemical processes. The results are expected to significantly contribute to the improvement and optimization of nature-inspired PEM fuel cells.

ACKNOWLEDGEMENTS

I would like to thank Dr. Umit O. Koylu for mentoring and guiding me through this research work. I am extremely thankful to Dr. Ming C. Leu for supporting me and unfolding my capabilities during the course of this research project. I am thankful to Dr. Kakkattukuzhy M. Isaac for guiding me in the computational aspect of this research. I am grateful to the National Science Foundation (Grant #CMMI-1131659) for funding this research work. I am indebted to the Department of Mechanical and Aerospace Engineering at the Missouri University of Science and Technology for giving me an opportunity to be a part of this research institution and for funding my entire period of study. I am also grateful to all the other faculty members of the department who have contributed in my learning of technical skills and motivating me to endure the challenges involved with my research. Additionally, suggestions and discussions with Dr. Nannan Guo and Qichang Wang on the details of computations are much appreciated.

I would like to thank all my friends for being with me and making my M.S. studies a new learning and memorable experience. And last but not least, I would like to express my deepest gratitude to my parents, my brother and my entire family for encouraging me to explore the various technologies available and to take up a research project in fuel cells.

TABLE OF CONTENTS

Page

LIST OF ILLUSTRATIONS

Page

LIST OF TABLES

Page

1 INTRODUCTION

The increasing needs for energy from conventional sources have envisioned an urgency to explore clean and renewable energy. Hydrogen is an abundant source of energy available in various compounds in nature. The most common source of hydrogen is water and hydrocarbons. Since production of hydrogen from unclean sources of water is not much of an impediment as impurities add to conductivity, it looks assured to be a promising source of fuel for the future.

Internal combustion (IC) engines have been modified to run on hydrogen. Although the power output is not up to the expectation, it is still a possible alternative fuel with sufficient room for development. Fuel cells, on the other hand, use hydrogen directly and through the reaction of hydrogen and air for producing electricity, which is clean and to a considerable extent renewable. The only reaction product of fuel cells is water in both vapor and liquid form. Fuel cells have a high power density, large operating range, and low operation temperature. Unlike IC engines, which have a large power band, fuel cells have a comparatively smaller range of effective operation and therefore they are good for stationary electricity production, which can be used for automobiles or energizing homes. Consequently, fuel cells represent a promising piece of technology and they are indeed very easy to install and operate. Once fuel cells are put into operation, they virtually can run throughout the lifetime of the membrane at a steady load but unfortunately are not good enough for dynamic loading at which IC engines excel.

Fuel cells are of many types: Proton exchange membrane (PEM) fuel cell, Solid Oxide fuel cell (SOFC), Direct Methanol fuel cell, and Phosphoric Acid fuel cell, to name some. Table 1.1 Types of fuel cells shows the list of fuel cells along with their types and material types. Of them, PEM and SOFC fuel cells are the most commonly used fuel cells. PEM fuel cell uses a solid polymer as an electrolyte along with two porous carbon electrodes. A layer of catalyst, preferably platinum, is used between the electrolyte and electrodes to enhance reactivity. SOFC uses a ceramic electrolyte, which is ideal for operation at very high temperatures (800 ^{0}C). SOFC does not depend on the requirement of expensive catalysts like platinum. The high temperature entailed is beneficial for reaction of oxygen and hydrogen as a result of which the efficiency of SOFC's are in the range of 50 to 60%.

Table 1.1 Types of fuel cells

Type	**Fuel**	**Electrolyte Material**	**Operating Temperature (^{o}C)**	**Efficiency (%)**
PEMFC	H_2, Methanol, Formic Acid	Hydrated Organic Polymer	<90	40-50
AFC	Pure H_2	Aqueous Potassium Hydroxide	60-250	50
PAFC	Pure H_2	Phosphoric Acid	180-210	40
MCFC	H_2, CH_4, CH_3OH	Molten Alkali Carbonate	600-700	45-55
SOFC	H_2, CH_4, CO	Solid Ceramic (YSZ)	600-1000	50-60

PEM fuel cells are better than SOFC's because of their low temperature operation (around 80 ^{0}C). High temperature operations may cause considerable wear and tear on the equipment, increased start up times, and a possibility of polluting products. SOFC's are capable of running on hydrocarbon fuels whereas PEMFC's are limited to pure hydrogen. The current study is focused on the flow distribution characteristics of PEM fuel cell flow fields only.

A PEM fuel cell has 9 regions, namely cathode and anode channels (also called flow fields), cathode and anode current collectors, cathode and anode catalysts, cathode and anode gas diffusion layer (GDL), and a membrane (electrolyte), as shown in Figure 1.1.

The channels and current collectors together form the bipolar plates. The electrochemical reactions that occur within a PEM fuel cell are given by equations (1) and (2).

$$H_2 \rightarrow 2H^+ + 2e^- \quad (1)$$

$$\frac{1}{2}O_2 + 2H^+ + 2e^- \rightarrow H_2O \quad (2)$$

Equation (1) is an oxidation reaction while equation (2) is a reduction reaction. The oxidation reaction occurs at the anode while the reduction reaction takes place at the cathode. The anode releases protons that combine with the oxygen ions from the cathode to form water. The membrane permits the flow of ions across its surface to reach the opposite electrodes hence conducting current across the fuel cell. The electrodes also called as Gas Diffusion Layer (GDL), aid in the distribution of gases across the area of

the fuel cell and are also responsible for moisture control. The channels, also called as flow fields, are responsible for the distribution of reactants to the fuel cell in addition to effectively removing the product gases and water out of the fuel cell.

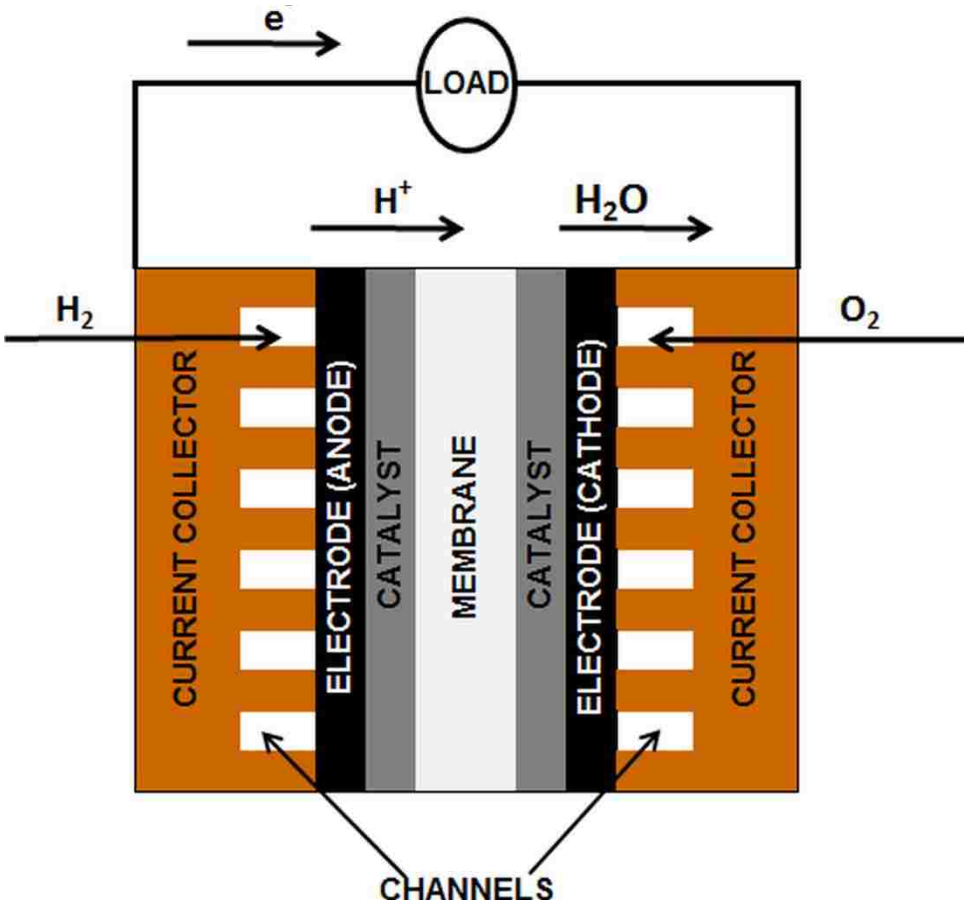

Figure 1.1 Schematic of a PEM fuel cell

A major quantum of fuel cell performance can be attributed to the efficiency of reactant and product distributions. A fuel cell has three operating regimes that are

representative of the losses present due to transport of reactants and products. The regions can be denoted on a polarization plot as shown in Figure 1.2, which is a typical performance characteristic plot for a fuel cell.

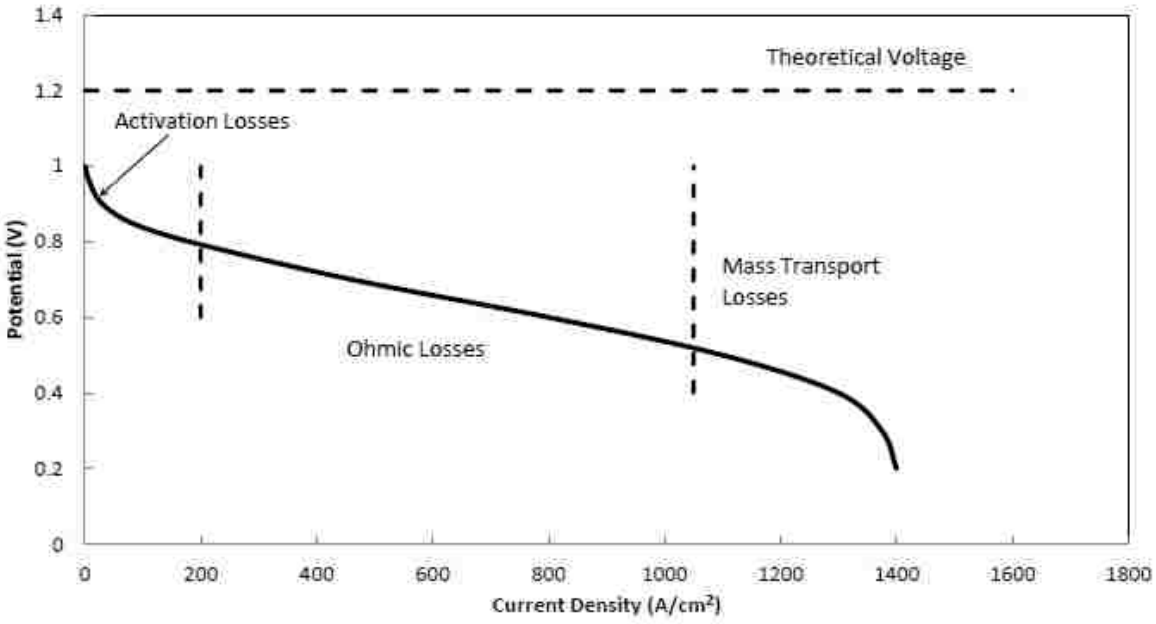

Figure 1.2 Polarization curve with the various losses present

The various losses present in a fuel cell operation are shown in Figure 1.2. The activation losses are a result of the electrochemical reaction, Ohmic losses are due to ionic and electronic conduction, and the mass transport losses are due to concentration transport inefficiencies. The various losses can be overcome with better materials, lesser contact resistances, and better flow field designs. The methods to overcome these losses have been discussed in detail in the cited literature. Flow field designs are the first place

to look for a solution to overcome the mass transport losses. Various conventional flow field designs like single serpentine, parallel, pin type, interdigitated, and a combination of one or more of the above constitute a majority of the commercially used designs. Figure 1.3 displays two of the commonly-used conventional designs. Each design has its own advantages and disadvantages that have been discussed in detail in the cited literature. Current research trends have implemented nature inspired designs to overcome certain limitations posed by conventional designs, namely reduced mass losses, reduced pressure losses, and better water management.

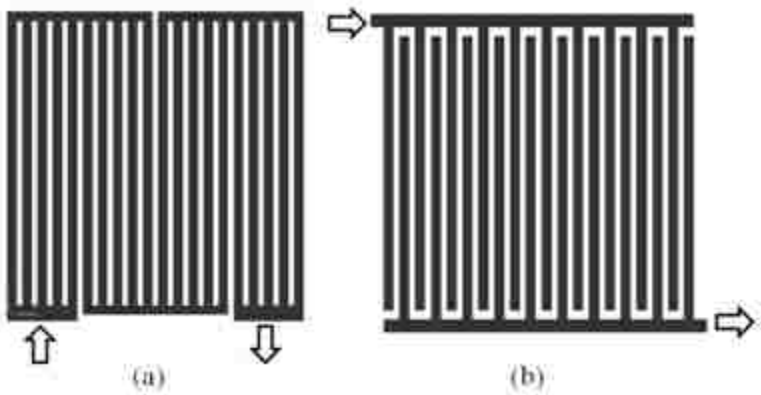

Figure 1.3 Conventional flow field designs a) parallel-in-series design b) interdigitated design

Nature has perfected its flow mechanisms over thousands of years and the knowledge of those designs gives a great insight of how to design better flow fields. The leaf and lung flow patterns are complicated yet efficient flow structures available in

nature illustrated in Figure 1.4. For example, the leaf has to convert carbon dioxide and water into carbohydrates in the presence of sunlight with the help of chlorophyll (photosynthesis). For this, the veins transport water and carbon dioxide from the roots and the trunk to the leaves and return the resulting carbohydrates back to the various cells of the plant. This process involves complex flow processes occurring in tandem and yet the efficiency of the system is significantly high.

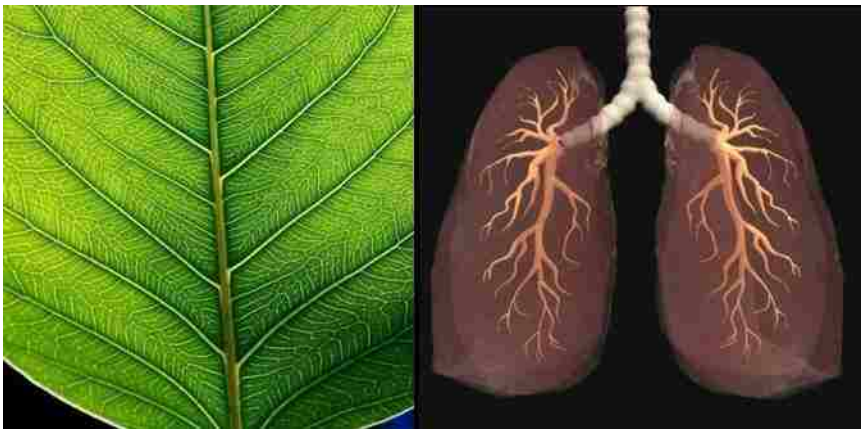

Figure 1.4 Leaf venation pattern (left), lung pattern (right)

Taking this as an inspiration, there have been various attempts at mimicking the flow structures and designing flow fields using mathematical laws relevant to these flow structures. The current research deals extensively with this new knowledge of nature inspired flow field designs. Finally, some of the relevant US Department of Energy goals have been summarized below.

The Department of Energy (DOE) is responsible for regulating the nation's energy goals and activities. Replacing IC engines with fuel cells in the transportation sector have been gaining momentum with the advancements in various aspects of fuel cell technologies. By 2017, it is envisioned to design a fuel cell with a 5000-hour life for powering transportation vehicles (e.g., buses and cars). There are also goals for all the components of a fuel cell as well as for the longer durability and cheaper costs. The membrane electrode assemblies available today are capable of producing 160mA/cm^2 at 0.8 V. It is expected to reach 300 mA/cm^2 at 0.8 V and a power density of 1 W/cm^2 by 2017. Bipolar plates, which are the structural backbones of fuel cells, are expected to have an electrical conductivity greater than 100 S/cm with a flexural strength greater than 25 MPa by 2017 [40]. The area specific resistance is to decrease from 0.03 Ω-cm^2 to 0.01 Ω-cm^2. Since the current technologies use a great deal of precious metal catalysts like platinum, it is aimed to reduce the platinum loading on low and medium temperature fuel cells. There have been research into iron based catalysts while biological enzyme based catalysts have also been explored [41].

2 REVIEW OF LITERATURE

A bipolar plate is an important part of a PEM fuel cell. It is responsible for distributing the reactant gases to the reaction sites, removing the product gases and liquid water from the fuel cell, collecting the generated current, and also providing structural rigidity to the fuel cell. Bipolar plates constitute up to 30% of the total cost of a fuel cell and amount to 60% of the weight of the fuel cell [1]. In addition, the bipolar plate significantly influences the fuel cell performance in two ways. Firstly, the electrical conductivity of the bipolar plate adds to the internal resistance of the fuel cell. Secondly, the transport efficiency of the bipolar plate greatly affects the transport of reactants and products within the fuel cell.

Most bipolar plates are conventionally made of metals like stainless steel, brass, aluminum, and sometimes copper. The issue with metals is the contact resistance between the metal surface and the gas diffusion layer (GDL). This interface is exposed to the various reactants and product gases as well as liquid water and impurities in the gases if any. This has a considerable chemical effect on the surface that results in increased contact resistivity. Considerable research has been done in studying the nature and magnitude of these resistances [2-5]. To overcome the problem of corrosion at metal surfaces, some work has been done in using carbon composite bipolar plates manufactured using selective laser sintering which reported good performance compared to bipolar plates manufactured by conventional processes [6].

The second issue was transport efficiency for which numerous solutions have been proposed in the existing literature. Two main methods of optimizing the flow structures have been identified. The first option is the modification of the channel

dimensions, including width, depth and channel shape that can yield good performance improvements. It was reported that high channel aspect ratios generated more uniform current distributions [7]. The effect of channel geometry is dependent on the operating conditions: the effect of the geometry was negligible at low current densities while it had a strong dependency at high current densities [8]. The second option is to modify the channel profiles. Non-standard profiles like fractals and spirals have been investigated. Fractals did not prove to be very efficient [9] whereas spiral designs showed a remarkable improvement over conventional designs [[10], [11]]. In addition, flow fields that mimicked natural structures were found to be a promising solution with improved pressure distribution and increased power density [[12]-[14]]. It was also suggested that a large part of the branching structures of cardiovascular and respiratory systems obeys Murray's law, which relates the radii of parent and daughter vessel diameters based on minimum energy expenditure [15].

It is known that water management presents one of the major hurdles in designing flow fields both conventional and nature-inspired fuel cells for efficient and durable operations. Water management is a very complex phenomenon that requires extensive investigation of the dynamics of water and the interactions between gas and liquid. The presence of relatively little amount of water causes membrane dehydration whereas excess water causes reactant starvation and also floods the fuel cell, both phenomena adversely affecting the performance. A literature review [16] detailed the issues of flooding and attempted to identify the causes of flooding and possible mitigation strategies. Various experimental techniques to detect flooding were also discussed in the same study. In understanding fuel cell flooding issues, knowledge of liquid and gas

interactions (multiphase flows) is of paramount importance. Multiphase flows are almost universally present in a PEM fuel cell. The applications of multiphase flows are indispensable in combustion processes, fluid transportation, oil and gas extraction, and in fuel cells in the present study. Fuel cells do not require atomizing the gases as in combustion applications and do not have very large flow velocities. Additionally, their channel dimensions are on the order of a few millimeters and hence they come under the micro-channel category.

Two-phase flows are a sub category of multiphase flows which are commonly observed in all PEM fuel cells. A recent review [17] discussed in detail the available in-situ and ex-situ methods of studying two-phase flows along with the advantages and disadvantages of each method. It also summarized to a large extent the various flow patterns observed experimentally. Numerical simulations are capable of predicting such flows but may be limited in their accuracy of predicting the flow patterns across the entire sandwich of the fuel cell. They have been able to predict the flows accurately one layer at a time by focusing on one part of the fuel cell at a time such as channels or GDL individually. A two dimensional CFD analysis conducted at the GDL interface to model the liquid dispersion [18] revealed the effects of pore saturation with liquid water on maximum current density. A three dimensional transport modeling approach for gas diffusion layers has been presented in [19]. A fingering and channeling mechanism of the liquid droplet transport through the porous layers of the GDL has been discussed in [20], which gave a deeper understanding of the underlying transport phenomenon.

The behavior of liquid water is also dependent on the hydrophilic or hydrophobic nature of the channel walls. It has been argued that walls that are more hydrophilic have

better water distribution characteristics [21]. Consequently, it is essential to observe the water distribution at the channel levels to get a better understanding of the water management capabilities of the flow field. Many methods are available for this purpose such as neutron imaging, X ray tomography, and direct visualization, to name a few. Neutron imaging is a very powerful but expensive method for observing the liquid water formation within a fuel cell. This method is particularly useful because of the neutron's sensitivity to hydrogen atoms present in water [22]. Neutron imaging was used to compare the water content in parallel, single serpentine and interdigitated flow fields; see for example [23]. Optical imaging was also used simultaneously to show the water dynamics within the channels. X-ray micro-tomography is a modification of medical computed tomography (CT) scanning. This technique was used successfully to observe the liquid water in the channels of a single serpentine channel and was also able to quantitatively determine the liquid water levels at the GDL interface [24]. Both of these two methods, however, are very complicated and expensive. On the other hand, due to its low cost and ease of data acquisition, an extensive literature is available on direct visualization using optical imaging systems, which require transparent fuel cell bipolar plates. For this purpose, metal can be used as the conductive gas distribution structure while a clear transparent back plate is used to directly observe the water formation as well as to provide rigidity to the fuel cell assembly.

Transparent fuel cells have been used extensively to directly observe the water formation in single serpentine channels. The effect of humidity at different operating voltages was recorded and a review of the various materials used for transparent PEM fuel cells were also presented in [25]. Liquid water transport in the cathode channels of a

transparent PEM fuel cell were visualized by operating the fuel cell at a relatively low temperature of 30 °C. It was observed that use of a hydrophilic cathode GDL had resulted in increased current density, which was attributed to a more uniformly hydrated membrane [26]. The effects of varying GDL materials and hydrophobicity were investigated, reporting that PEM fuel cells with untreated GDLs were prone to film and slug formations within the cathode channels [27]. The water flooding and two-phase flow characteristics of the cathode channels for interdigitated, cascade and parallel flow fields were also observed. It was concluded that flooding occurred much faster in the parallel channels compared to the interdigitated and cascade channels [28].

Based on the observation that nature has developed efficient mass transport systems, two recent studies [[29], [30]] suggested a number of bio-inspired flow field designs for use in PEM fuel cells and compared their polarization curves. It was reported that bio-inspired flow fields improved the fuel cell performances due to better distributions of reactants. However, no details about their water handling capabilities were offered.

The main objective of the present research is to investigate a bio-inspired design in detail, especially with respect to its water management capabilities, so that a comprehensive understanding can be developed for future improvements and optimizations. In particular, a transparent PEM fuel cell assembly was designed and constructed for direct visualization of liquid water in flow channels. By mimicking the natural structures such as a leaf, an interdigitated bio-inspired fuel cell involving the Murray's law for the branching channels was manufactured. The performance of this biologically-inspired fuel cell was evaluated by measuring the voltages at different

currents and then plotting the corresponding polarization and power density curves. Since such limited experiments are not sufficient to explain what happens inside the fuel cell and therefore can only represent the tip of the iceberg, it was essential to supplement the performance curves with additional measurements and computations. Experiments included direct visualization of liquid water by digital photography at various fuel cell operating conditions so that water management capabilities of the bio-inspired flow design could be quantified and clearly linked to its performance. The water flow dynamics were recorded while the different types of flow regimes were also identified based on the two-phase flows in micro-channels. While there are numerous studies in the literature on direct water observations and water management capabilities of conventional PEM fuel cells (see [22] and references cited therein), this is the first study, to our knowledge, that considers the same for a bio-inspired flow configuration. The present experiments were complemented with advanced computations by adopting a commercial software package (ANSYS Fluent) that provided predictions of pressure, velocity, reactant (hydrogen and oxygen) and product (water) distributions within the fuel cell. The simulations were compared to experimental results in order to validate predictions by identifying similarities and differences. The same experiments and computations were also repeated for a single-serpentine PEM fuel cell so that the present bio-inspired design could be compared to a conventional design for quantifying the improvements relative to the existing flow field designs. While the present study contributes to the general goal of significantly improving performance, it also paves the way for proper optimization of bio-inspired flow fields in PEM fuel cells.

3 BIO-INSPIRED DESIGNS

3.1 THEORETICAL DESIGN

Recent research has suggested that nature inspired flow field designs have superior performance capabilities. It is a known fact that nature has been able to achieve effective mechanisms to transport food and nutrients across great distances with minimal losses. The vein and cardiovascular structures in plants and mammals are classic examples. Based on the available literature and some novel ideas, Guo et al. [29], formulated a bio-inspired design which was shown to have higher power density characteristics compared to conventional designs. Numerical simulations were presented to support their findings. The root cause of the increased performance of those designs was hinted as better water management but not documented. Water management is highly dependent upon the two-phase flow aspects of the design. Murray's law was beneficial in determining the minimum required dimensions of the channels for transport of liquid and gas species from the primary channels through to the outlets via secondary channels. In the process of eliminating redundancies, an interdigitated design was found to be the most practical design. Additionally, the channel areas must be comparable to their conventional counterparts (Table 3.1). These considerations were made so as to eliminate the external factors and focus only on the flow field geometry as the primary focus of study. Figure 3.1 displays the resulting flow field designs used for the experiments and simulations. Arrows indicate the direction of gas flow through the corresponding inlets and outlet channels for the designs.

Table 3.1 Channel area comparison

	Single serpentine	Bio-inspired
Total face area	2500 mm^2	2500 mm^2
Channel face area	1274.00 mm^2	1219.37 mm^2
Channel area ratio	50.96%	48.7%

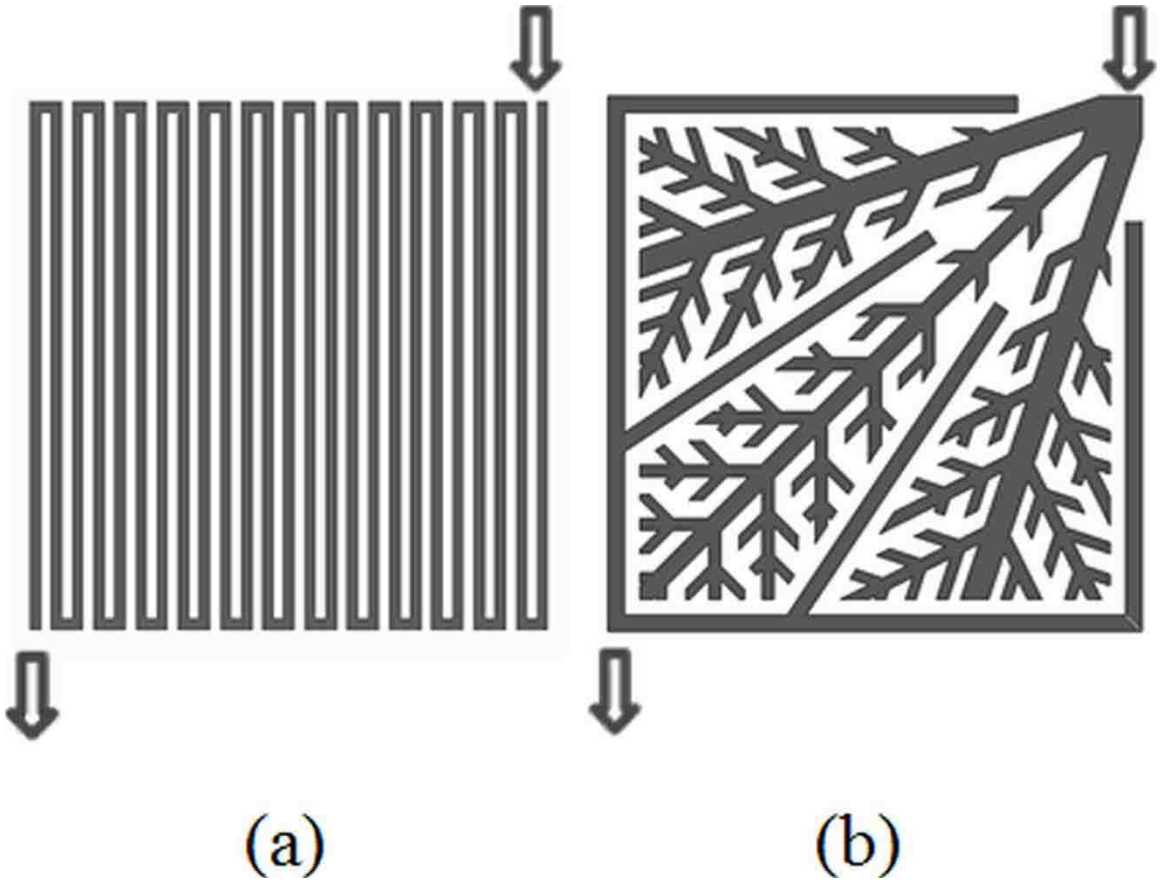

Figure 3.1 Flow field patterns, (a) single serpentine (b) bio-inspired Murray's law design

3.2 BIPOLAR PLATE DESIGN

Bipolar plates apart from being the heaviest and most expensive single component of the fuel cell, is the second most critical component of a fuel cell after the MEA. The MEA is the heart of the fuel cell but the bipolar plate behaves as the skeletal and circulatory system of the fuel cell. As a matter of fact, a great deal of research has gone into the optimization of material and manufacturing processes of bipolar plates [[6], [13], and [14]]. Flexural strength, conductivity and corrosive resistance are the most important material properties of a bipolar plate for which recommended values [40] are as follows: a minimum of 25 MPa flexural strength and 1 kS/cm conductivity, and a corrosion resistance lesser than 0.016 mA/cm^2. In addition to these requirements, practical requirements including low cost and weight and machinability are to be considered. For this study, transparency was necessary for observing liquid water formation within the channels. Many of the known transparent materials are bad conductors of electricity. Thus it was decided to use a bilayer bipolar plate that consisted of (i) the current collector and channels machined from copper, (ii) transparent back plate made from Lexan®. Copper was considered for its excellent electrical conductivity. Stainless steel was extremely hard to machine and therefore copper was a practical choice, especially considering the spindle speed limitation of the CNC mill available in the Department of Mechanical and Aerospace at Missouri University of Science and Technology. Corrosion would be an issue but care was taken to minimize corrosion during lead times between experiments.

In this way, the copper channels would also perform the part of the current collector where they would collect the current from the reactions through tabs connected

to the load bank. It was also later observed that the thermal conductivity of copper was very much beneficial in the successful running of experiments as the channel walls would become warm by absorbing heat from the influx of hot inlet gases. This reduced the condensation on the Lexan surface, thus reducing the uncertainty in identifying liquid water within the channels.

1.5 mm thick copper sheets and ¼ inch Lexan sheets were used for the bipolar plate. Loctite E360 epoxy was used as the adhesive between the copper and Lexan surfaces. The epoxy was allowed to cure for 72 hours with a uniform loading of 196.2 N. The 1.5 mm thick copper plate was then machined on a 3-axis CNC mill with 0.8 mm diameter uncoated carbide end-mill. The depth of cut was 0.00984 inches per pass and a total of 8 passes were required to reach a depth of 0.0787 inch or 2 mm. This was to remove a part of the epoxy layer in order to ensure clear unobstructed view of the channels.

3.3 MURRAY'S LAW

Murray's law is the natural law that defines branching in most natural distribution systems. It is based on the principle of minimum work required for a vein of a specified diameter to transport a given fluid. Table 3.2 summarizes the nomenclature used for the mathematical representation of Murray's law. The derivation of Murray's law has been described in detail in references [[15], [30], [38] and [39]]. A summary of the literature has been presented below.

Murray's law assumes that there are two terms that contribute to the loss of energy associated with sustaining blood flow in any section of a vessel: (a) energy required to overcome viscous drag in a fluid (b) metabolic energy required to maintain blood volume and vessel tissue. A simplified analysis involves the consideration of the vessel segments as circular pipes or radius *r* and length, *L*.

Table 3.2 Nomenclature for Murray's law

Δp	Pressure drop	P_v	Viscous Power Loss per Unit Length
L	Path Length	Q	Volumetric Flow Rate
r	Path Radius	μ	Dynamic Viscosity
k_m	Metabolic Constant	P_m	Maintenance Power Loss per Unit Length
P	Power to Maintain Blood Flow	X	Branching Parameter
A_c	Cross-Sectional Area of Channel	p	Channel Perimeter
W	Channel Width	D	Channel Depth
d^H	Hydraulic Diameter	N	Number of Daughter Branches

The power required per unit length to overcome viscous drag across a segment can be represented as shown in equation (3)

$$P_V = \left(\frac{\Delta p}{L} \right) Q \tag{3}$$

The Hagen-Poiseuille equation (4) can be used to solve for the volumetric flow rate in a pipe with fully-developed laminar flow.

$$Q = \frac{\pi r^4 \Delta p}{8 \mu L} \tag{4}$$

Substituting the pressure drop from equation (3) in (4) results in the expression of power requirement for overcoming viscous drag as denoted in equation (5).

$$P_V = \frac{8 \mu Q^2}{\pi r^4} \tag{5}$$

Equation (6) is the expression for the required metabolic power per unit length to maintain blood cells and walls of the vascular system. In fact, Murray assumed that the power required to sustain metabolic requirements of a system could be related directly to volume of each segment.

$$P_m = k_m \pi r^2 \tag{6}$$

The summation of equations (5) and (6) give the total power required to maintain blood flow through the vascular system. Differentiating the resulting power equation with respect to the radius of the system and equation to zero yields the minimum power consumption for a given flow rate *Q* as expressed in equation (7).

$$\frac{dp}{dr} = -\frac{32 \mu Q^2}{\pi r^5} + 2 \pi k_m r = 0 \tag{7}$$

When the above equation is solved for the flow rate, it generates the expression in equation (8). It can be inferred from the equation that the only variable is *r*. Hence the optimum value of the radius of the vessel for a given flow rate can be calculated from the expression.

$$Q = \frac{\pi}{4}\sqrt{\frac{km}{\mu}}r^3 \tag{9}$$

The application of the continuity principle here at the junction at which the daughter branches bifurcate from the parent branches yields in an expression relating the radii of the daughter branches (r_{ch}) to the total mass flow rate in the parent branches. The continuity principle states that the total mass flow rate entering a vessel is equal to the sum of the mass flow rates of fluid exiting the daughter vessels. The resulting expression is shown in equation (10).

$$Q_{par} = \frac{\pi}{4}\sqrt{\frac{km}{\mu}}r^3 = \sum_{i=1}^{N} Q_{ch,i} = \frac{\pi}{4}\sqrt{\frac{km}{\mu}}\sum_{i=1}^{N} r^3{}_{ch,i} \tag{10}$$

A simplification of equation (10) results in equation (11) which directly relates the radii of the parent branches to the sum of the daughter branches.

$$r^3{}_{par} = \sum_{i=1}^{N} r^3{}_{ch,i} \tag{11}$$

Equation (11) is the Murray's law expressed in the form of radii. The expression in the form of diameters results in equation (12).

$$d^3{}_{par} = \sum_{i=1}^{N} d^3{}_{ch,i} \tag{12}$$

Assuming a constant branching parameter at each bifurcation, the diameter of the N^{th} branch can be obtained from the expression in equation (13) where X is the number of branches required from the N^{th} generation to satisfy the continuity principle.

$$d^3{}_N = \frac{d^3{}_{par}}{X^{N/3}} \tag{13}$$

Finally, for rectangular channel cross-sections, the hydraulic diameter can be obtained by using equation (14) where *W* and *D*, are the channel widths and depths respectively. This is particularly useful for PEM fuel cells where the channels are rectangular.

$$d^H = \frac{4A_c}{P} = \frac{WD}{W+D} \tag{14}$$

4 METHODOLOGY

4.1 EXPERIMENTAL METHODS

Transparent bipolar plates were manufactured to enable the visualization of water formation within the channels. The dimensions of the fuel cell are listed in Table 4.1.

Table 4.1 Transparent fuel cell dimensions

Cell width	50 mm
Cell height	50 mm
Bipolar plate thickness	7.92 mm
Channel depth	2 mm
GDL thickness	0.3 mm
Catalyst layer thickness	0.01 mm
Membrane thickness	0.05 mm

The fuel cells were tested on a fuel cell test rig (Greenlight Innovations G40), which is shown in Figure 4.1. The system has controls for regulating the gas flows, inlet temperatures of gases and humidification, cathode and anode backpressure sensors, end plate heaters, and capability to set voltage or current set points to obtain performance data. There are sensors that detect hydrogen gas leakage and stop the machine operation when the alarms go off.

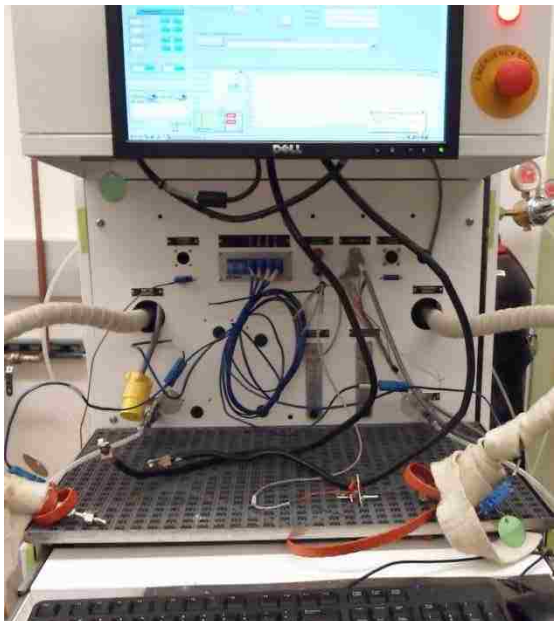

Figure 4.1 Greenlight Innovations G40 Test Rig

Figure 4.2 shows a schematic of the fuel cell test rig. The hydrogen and air entered the humidifiers via mass flow controllers and relief valves. The air was first humidified and passed through the fuel cell. The load bank generated an electrical load for the fuel cell and also recorded the voltage, current densities, and power densities. The thermocouples recorded the end plate temperature as well as the gas temperatures. The high resolution camera took images of the fuel cell at specified intervals.

The general fuel cell assembly is shown in Figure 4.3. In this case, the current collector and channels were one single plate (copper bonded to Lexan) and a silicon gasket of 15 mm thickness was used to enclose the membrane. Tabs were machined on the copper plate for current collection and voltage measurement. The fuel cell was then assembled with sufficient clamping pressure on the end plates to ensure a good seal.

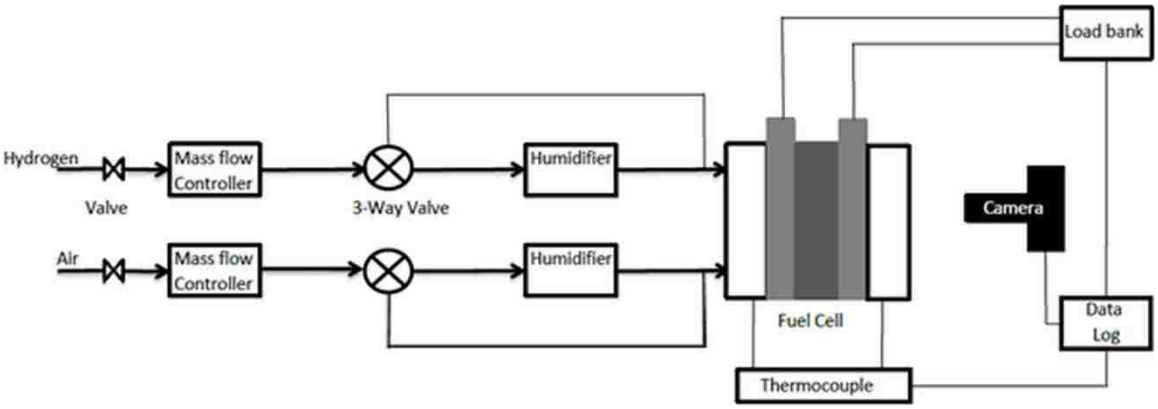

Figure 4.2 Schematic of the fuel cell test rig

The fuel cell assembly was then rigged to the machine with the anode as the negative terminal and cathode as the positive terminal. All connections were secured to ensure no hydrogen leaked during operation. The fuel cell was allowed to reach steady state which typically took 1 hour. The operation parameters for the experiment are listed in Table 4.2.

Once the fuel cell reached steady-state conditions, the current density was ramped up in increments of 40 mA/cm^2. The fuel cell was allowed to stabilize at each current density set point and then readings were taken. Polarization curve were obtained by repeating the experiments and recording the corresponding voltages at various current densities.

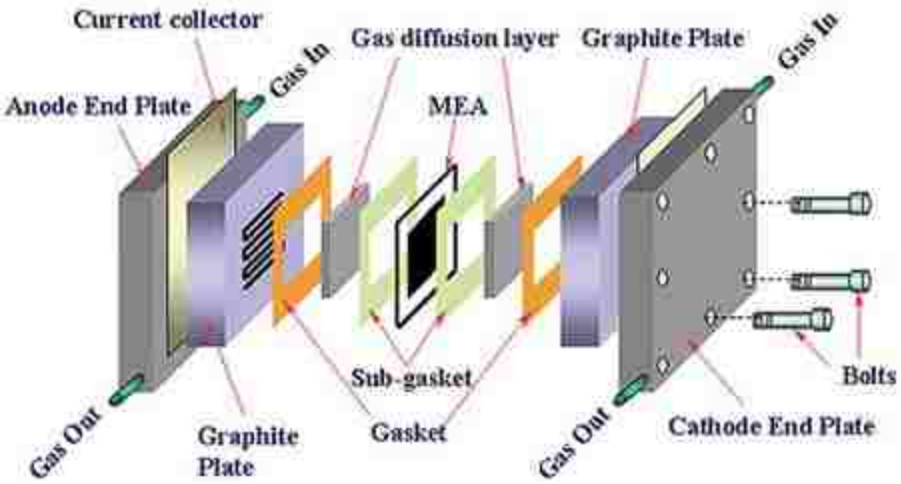

Figure 4.3 Schematic of a generic PEM fuel cell

Table 4.2 Operation conditions for PEM fuel cell

Operating temperature (K)	343
Operating pressure (kPa)	101.3
Inlet flow rate (sccm)	300
Outlet flow rate (sccm)	1000
Relative humidity	100%

The experimental setup is shown in Figure 4.4. A high resolution camera with a macro lens was used to take images and videos of the water formation within the channels. Images were later processed and analyzed to understand the dynamics and behavior of water in fuel cell micro-channels. The camera used was a Canon EOS 7D, with a 28-135 mm lens system.

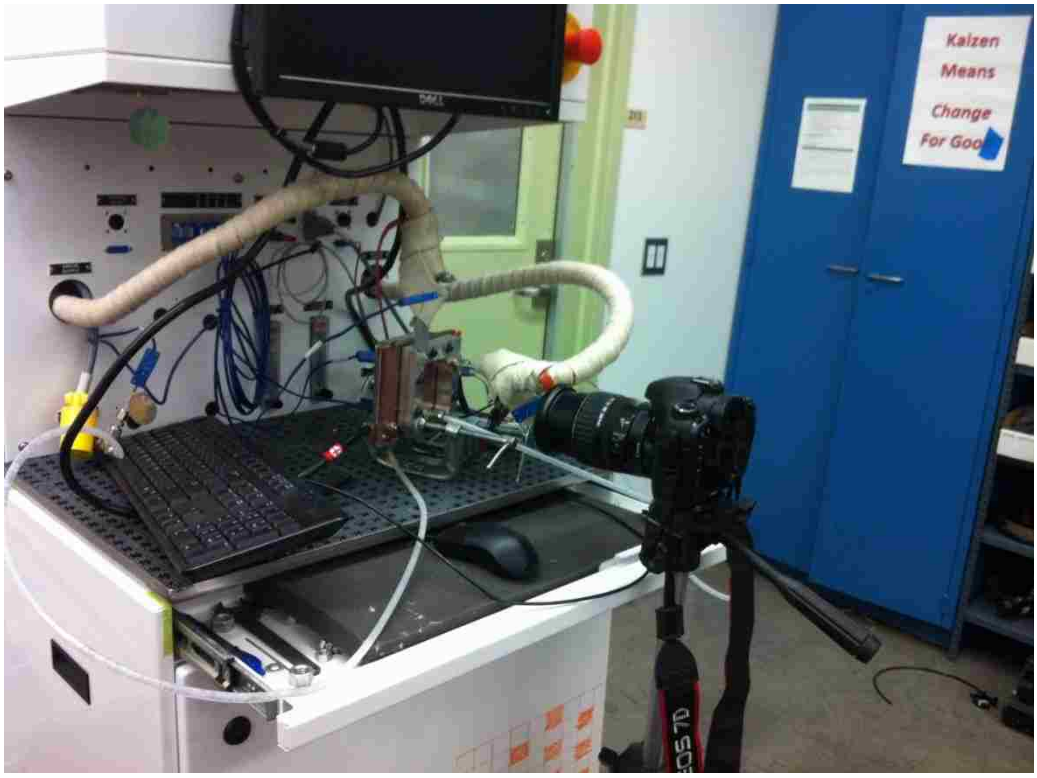

Figure 4.4 Fuel cell test setup for direct visualization with high resolution digital camera

4.2 COMPUTATIONAL METHODS

Fuel cell technology cuts across multiple disciplines including materials, mass and energy transport, manufacturing, and chemistry because of the diversity and complexity of electrochemical reactions and transport phenomena. Advanced modeling and simulation is crucial to effectively design and optimize fuel cell technologies with high efficiency, low cost, and extended durability by elucidating the underlying physical and electrochemical processes observed from the experiments. Computational fuel cell dynamics also provide the essential tools to accurately predict fuel cell performance

characteristics and therefore to significantly reduce the time and expense of prototyping and testing in various military and industrial applications.

4.2.1 Geometry Formulation. The flow field designs were generated using NX CAD software. The CAD designs were meshed using Gambit, a pre-processor program for meshing. Post-processing and numerical simulations were then carried out using Ansys Fluent 14.0®. The bio-inspired geometry was designed primarily using Murray's law to define the branching parameters. The shape of the geometry was obtained by imitating the vein structure of a leaf. There were three primary channels followed by secondary and tertiary branches. Table 4.3 summarizes the branch dimensions. Figure 4.5 shows the final bio-inspired design with an overall depth of 2 mm**.**

Table 4.3 Dimensions of the various branches of the bio-inspired flow field

Branches	Generation	Hydraulic diameter (mm)	Channel width (mm)
Right & left branches	1st 2nd 3rd	1.88 1.35 1.20	2.51 1.23 1.00
Middle branches	1st 2nd 3rd	1.63 1.29 1.20	1.78 1.14 1.00

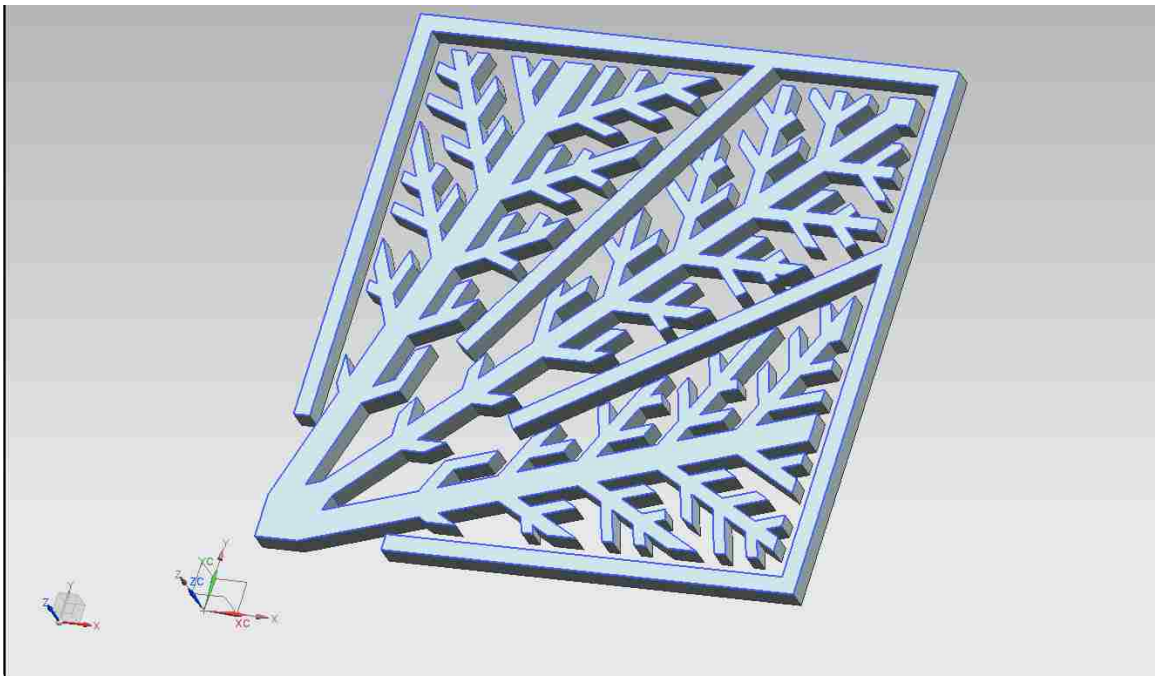

Figure 4.5 3D image of bio-inspired flow field

4.2.2 Meshing. A parasolid file was first imported into Gambit from NX. The parasolid file was then extruded layer by layer to generate the GDL, membrane, and catalyst layers. A mesh size of 0.5 mm was selected. The channels had 10 nodes along the thickness while the current collector had 5 nodes. The GDL, catalyst and membrane had 5, 4, 4 mesh elements along their thicknesses, respectively. In addition, no-flow portions of the fuel cell did not need large mesh densities. Smaller mesh sizes e.g. 0.25 mm were deemed unnecessary as they did not provide significant increase in result accuracies.

During meshing, node matching had to be ensured because an inconsistent mesh would cause the merging of volumes to fail that would result in inappropriate

simulations. The bio-inspired design being a non-standard geometry, it had to be split into smaller volumetric fragments for better control over meshing. For example, the channel face was split into three regions: inlet gas flow channel region, land region and outlet channel regions. The resulting sub-volumes were meshed individually and finally merged into a single entity representative of the channel of a fuel cell. Figure 4.6 shows the mesh consistency on the land and outlet channel boundaries. The nodes on the left image did not match, causing an inconsistent mesh while they matched perfectly in the right image.

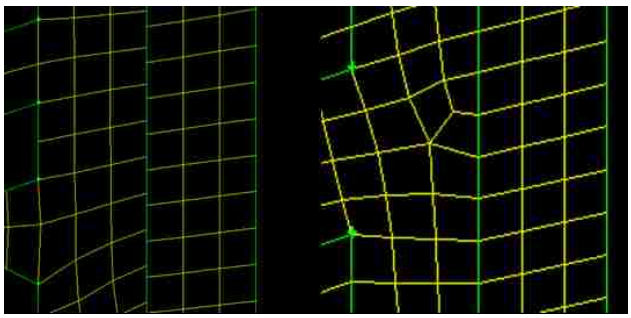

Figure 4.6 Mesh inconsistent (left), consistent (right)

The meshing scheme on the inlet channels and the land area was quadratic pave whereas the outlet channel was meshed using a quadratic sub map scheme. This difference in meshing scheme was inevitable due to the complexity of the design. It was observed that meshing the outlet channel and the inlet channels first followed by the land areas delivered a consistent mesh, as shown in Figure 4.7 and Figure 4.8.

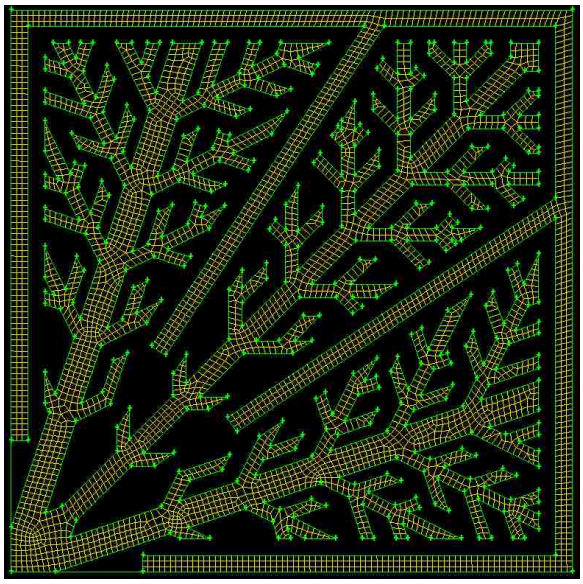

Figure 4.7 Meshed inlet and outlet faces

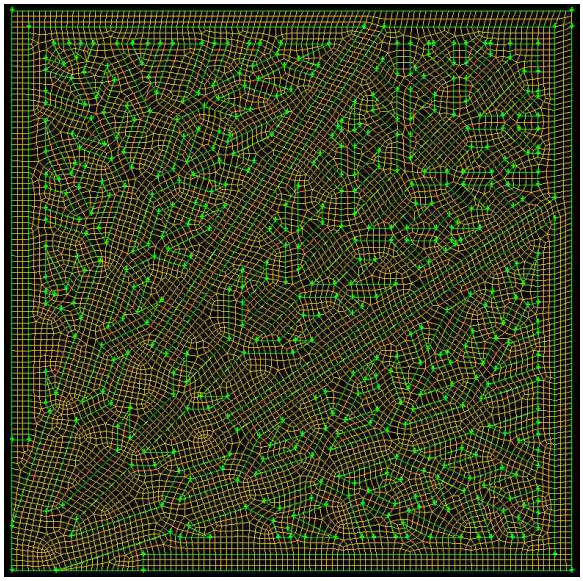

Figure 4.8 Full GDL face mesh with 0.5 mm element size

Similarly, each volume corresponding to the channels, current collectors, catalyst and membranes were meshed with a size of 0.5 mm. The unmeshed fuel cell is shown in

Figure 4.9 while the meshed fuel cell is shown in Figure 4.10. After the meshing is complete, the faces were defined and zones were allocated based on their functionality. Current collector had no flow and hence was set as a solid zone while the remaining parts of the cell were set to fluid zones.

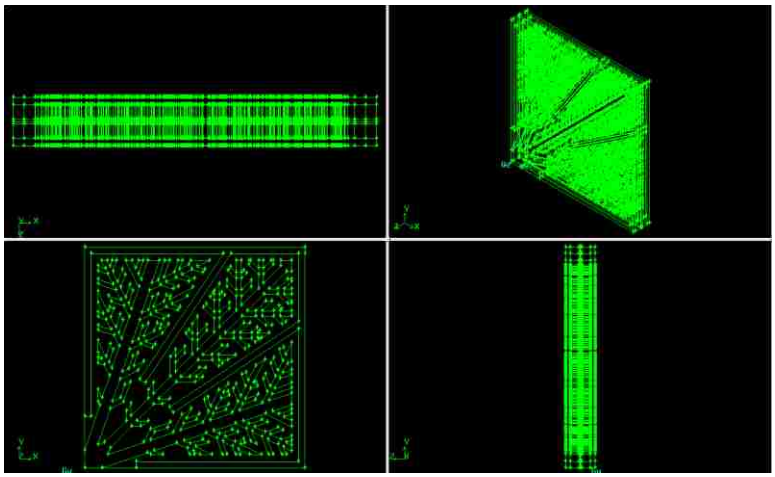

Figure 4.9 Fuel cell with all 9 regions

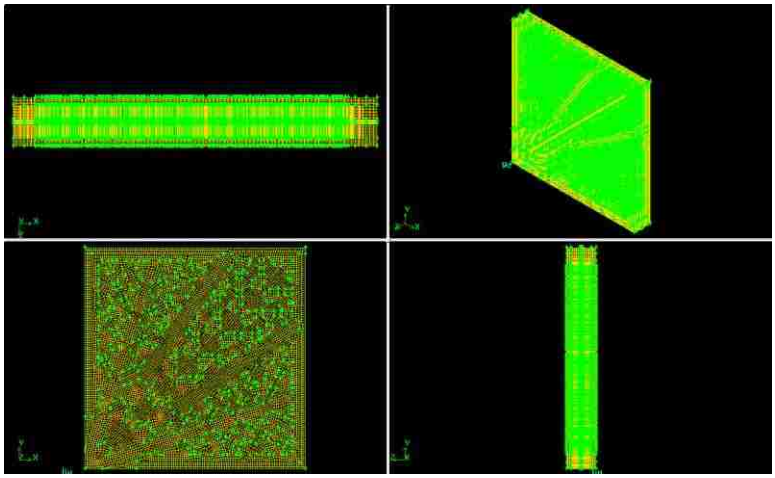

Figure 4.10 Fuel cell with all 9 parts meshed

Table 4.4 shows the boundary type definitions while Table 4.5 shows the zone definition for the fuel cell.

Table 4.4 Definition of boundary types

Face	**Boundary condition**
Anode and cathode inlets	Mass flow inlet
Anode and cathode outlets	Pressure outlet
Anode and cathode current collector top faces(terminals)	Wall
All external faces of current collector, GDL, channels, membrane and catalyst excluding all interfaces between GDL-channel, GDL-catalyst and catalyst-membrane.	Wall

Table 4.5 Definition of zone types

Zone	**Material type**
Current collectors	Solid
Channels	Fluid
GDL	Fluid
Catalyst	Fluid
Membrane	Fluid

4.2.3 Computations. The fuel cells module of the ANSYS Fluent modeling software was used to conduct the simulations. A set of equations specific to fuel cell electrochemistry and fluid dynamics were used to predict the performance. The

nomenclature used for the following equations is listed in Table 4.6. A summary of the equations used to predict the performance has been listed below.

Table 4.6 Nomenclature for simulations

ϕ	Transported quantity	t	Time
A	Superficial qrea	V	Volume
Γ_ϕ	Diffusivity of transported quantity	σ	Electrical conductivity
φ	Electrical potential	R	Volumetric transfer current
r_w	Condensation rate	ρ	Density
s	Saturation	$\overrightarrow{V}$	Velocity profile
k	Permeability	P_c	Capillary pressure
ε	Porosity	μ	Kinematic viscosity
S_i	Source term for Navier-Stokes equations	C_2	Inertial resistance
v_i	Velocity in the i direction	v_{mag}	Velocity magnitude
r_s	Pore blockage exponent	T	Temperature
D	Diffusivity	P	Pressure
R	Reaction Rate	i	Current density
F	Faraday's constant	R	Ideal gas constant
M	Mass	γ	Activity coefficient
α	Charge transfer coefficient	η	Overvoltage
an	Subscript for anode	cat	Subscript for cathode
ref	Subscript for reference values	l	Subscript for liquid water

Equation (15) is the conservative form of the Navier-Stokes transport equation which is used to solve for the fluid flow and heat transfer in a PEM fuel cell.

$$\frac{\partial}{\partial t}\int_V \rho\phi dV + \oint_A \rho\phi\vec{V}\cdot dA = \oint_A \Gamma_\varphi \nabla\varphi \cdot dA + \int_V S_\phi dV \tag{15}$$

The first term of equation (15) is the transient term while the second term is the convective transport term. The third term represents diffusion and the fourth term is a source term.

Since PEM fuel cells operate at low temperatures, the condensation of water is to be modeled. Liquid water helps keep the membrane hydrated but also blocks the gas diffusion layer pores, retarding diffusion rates and reducing active reaction sites.

Equations (16) and (17) were used to determine the saturation based on the condensation rate and the difference between partial pressure of water and the saturation pressure.

$$\frac{\partial(\varepsilon\rho_l s)}{\partial t} + \nabla\cdot(\rho_l\vec{V}s) = r_w \tag{16}$$

$$\frac{\partial(\varepsilon\rho_l s)}{\partial t} + \nabla\cdot(\rho_l \frac{ks^3}{\mu_l}\frac{dp_c}{ds}\nabla s) = r_w \tag{17}$$

The first equation is applicable to all regions except the GDL whereas the second equation is relevant only to the GDL. The second term in equation (18) uses capillary diffusion as the primary transport mechanism, which more accurately emulates conditions within the GDL.

$$\nabla\cdot(\sigma\nabla\varphi) + R = 0 \tag{18}$$

Equation (18) was to be solved for the surface over-potential for which two potential equations were solved for both solid and membrane phases separately. The exchange current densities were obtained from the Butler-Volmer equations listed below (equations 19a and b).

$$R_{an} = i_{ref}^{an} \left(\frac{[H_2]}{[H_2]_{ref}} \right)^{\gamma_{an}} \left(e^{\frac{\alpha_{an} F \eta_{an}}{RT}} - e^{\frac{-\alpha_{cat} F \eta_{an}}{RT}} \right) \quad (19\ a)$$

$$R_{cat} = i_{ref}^{cat} \left(\frac{[O_2]}{[O_2]_{ref}} \right)^{\gamma_{an}} \left(e^{\frac{\alpha_{an} F \eta_{cat}}{RT}} + e^{\frac{-\alpha_{cat} F \eta_{cat}}{RT}} \right) \quad (19\ b)$$

Source terms account for the various reactions taking place and the relevant losses within the fuel cell. Hydrogen and oxygen are both consumed whereas water is the product in a PEM fuel cell. Hence, hydrogen and oxygen are represented by negative source terms whereas water is represented by a positive source term for the resultant product creation. The Stefan- Maxwell equations (20a- 20c) provide the reaction source terms.

$$S_{H_2} = -\frac{M_{w,H_2}}{2F} R_{anode} \quad (20\ a)$$

$$S_{O_2} = -\frac{M_{w,O_2}}{4F} R_{cathode} \quad (20\ b)$$

$$S_{H_2O} = \frac{M_{w,H_2O}}{2F} R_{cathode} \quad (20\ c)$$

Since the GDL and catalyst are porous regions, there are viscous losses, which are proportional to the local fluid velocity within the region. Equation (21) is the source term representing viscous losses within the porous layers of the fuel cell.

$$S_i = -(\frac{\mu}{k} v_i + C_2 \tfrac{1}{2} \rho v_{mag} v_i) \tag{21}$$

Not all chemical energy released is converted to electrical work due to irreversibility of the process. Consequently, a volumetric source term for thermal energy is also incorporated as shown in equation (22).

$$S_h = h_{react} - R_{an,cat} \eta_{an,cat} + I^2 R_{ohm} + h_L \tag{22}$$

The first term represents the net enthalpy change due to the electrochemical reactions and the second term is a product of the anode and cathode exchange current densities and over potentials in the porous regions. The third and fourth terms are the ohmic resistivity of the conducting media and enthalpy change due to vaporization and condensation of water, respectively.

The diffusivities of the species were calculated using the dilute approximation method as shown in equation (23), which accounts for both the porosity of the porous media and the pore blockage exponent.

$$D_i = \varepsilon^{1.5} (1-s)^{rs} D_i^{ref} (\frac{p_{ref}}{p})(\frac{T_{ref}}{T})^{1.5} \tag{23}$$

The operating conditions and simulation parameters are listed in Tables 4.7 and 4.8, respectively.

Table 4.7 Operating conditions for PEM fuel cell simulation

Operating temperature (K)	343
Operating pressure (kPa)	101.3
Inlet flow rate (sccm)	300
Outlet flow rate (sccm)	1000
Relative humidity	100%

Table 4.8 Parameters for the simulation model

Reference exchange current density at anode (A/m^2)	4.48×10^{5}
Reference exchange current density at cathode (A/m^2)	4.48
Charge transfer coefficient at anode	1.0
Charge transfer coefficient at cathode	1.0
Concentration exponent at anode	0.5
Concentration exponent at cathode	1.0
Open circuit voltage (V)	0.98
H_2 diffusivity (m^2/s)	8.0×10^{-5}
O_2 diffusivity (m^2/s)	2.0×10^{-5}
H_2O diffusivity (m^2/s)	5.0×10^{-5}
Membrane equivalent weight (kg/kmol)	1100
Catalyst layer surface-to-volume ratio (1/m)	1.25×10^{7}
GDL electric conductivity ($1/\Omega$ m)	280
GDL porosity	0.82
GDL viscous resistance at anode ($1/m^2$)	1.0×10^{12}
GDL viscous resistance at cathode ($1/m^2$)	3.86×10^{12}
GDL and catalyst layer permeability ($1/m^2$)	5.68×10^{10}
Bipolar plate electric conductivity ($1/\Omega$ m)	5.8×10^{7}
Contact resistance (Ω m)	6×10^{6}

The values adopted for the simulation were obtained from previous literature. The contact resistance is representative of the electrical resistance between the current collector and GDL surface.

5 RESULTS AND DISCUSSION

5.1 GENERAL PERFORMANCES AND COMPARISONS

Polarization curves and power density curves were plotted for the operating conditions specified in Table 4.2. A polarization curve is a plot of cell voltage against current density for a PEM fuel cell. The curve can be obtained by varying the current density (load) and recording the voltage across the cell. The polarization curve is the first and foremost criteria for measuring the performance of a fuel cell by quantifying the major losses that cause the fuel cell voltage to be lesser than the thermodynamically-ideal value (reversible voltage). A polarization curve can be divided into three regions representing the three major losses in a fuel cell, namely, activation losses, ohmic losses, and mass transport losses, as generically shown in Figure 1.2. In the first region, activation losses occur as a consequence of the energy expended for reactions to overcome the activation barrier, resulting in a voltage drop. Activation losses dominate at relatively low currents/high voltages. The second region is the ohmic losses region, also termed as charge transport region, in which, the ions are transported across the membrane and towards their corresponding electrodes. An electric resistance is induced owing to the material properties at the membrane, catalyst, gas diffusion layers, and current collectors. All these resistances being in series sum up and impede the free movement of ions. The third type of losses represented on the polarization plot is the mass transport losses, which dominate at relatively high currents/low voltages. Diffusion of reactants and product fluxes across the membrane in addition to liquid water entrapment within the electrodes generate significant performance losses and operational instability. The next measure of a fuel cell performance is the power density curve, which plots the power

density against the current density. The power density can be defined as the power produced per unit electrolyte area and mathematically represented as the product of voltage and current density. A fuel cell capable of producing high power densities at relatively wider range of current densities is preferred which can be obtained with effective fuel cell flow field designs.

The experimental performance of the present bio-inspired design is illustrated and compared to the conventional single serpentine design in Figure 5.1. The measured variations of cell voltage with current density for both types of PEM fuel cells followed a typical polarization curve, in which three distinct regions of activation, ohmic and concentration losses can be clearly identified. Starting with nearly identical open circuit voltages (OCV) and around 1 V, the voltages dropped with increasing current, as expected, for both fuel cells. As can be seen from Figure 5.1, the bio-inspired flow design always yielded a higher voltage at a given current with the difference in performances increasing with current density. At lower current densities, the performance difference was marginal: for example at 350 mA/cm^2, the bio-inspired flow field design gave approximately 10% higher voltage compared to its conventional counterpart. The enhancement increased to 40% at 650 mA/cm^2, indicating a substantial voltage improvement at high current densities. This observation is consistent with other studies that, reported that the effect of flow field design had little significance at lower current densities in contrast to the substantial effect at higher current densities [31]. This is due to the fact that the reaction rates are low at low current densities, resulting in lower water content within the electrolyte and flow fields. When the product water content is low, it appears as droplets of varying sizes that are quickly evaporated due to the flowing hot

reactant gases. These droplets pose little restriction to the flow consequently giving little room for performance improvements with flow field designs. But at higher current densities, the geometry of the flow field plays an important role as the restrictive effects of large water columns and boundary flow inhibiting reactant and product flux distribution come into play. Thus, the bio-inspired design distributes the reactants better and expels the products efficiently, in turn reducing the mass losses at high currents.

Similar observations can be extended to the power density curves shown in the second part of Figure 5.1. A 30% higher peak power density was obtained for the bio-inspired design compared to the single serpentine design. This improvement was seen at 600 mA/cm^2 for the bio-inspired design compared to a peak power density at 480 mA/cm^2 for the single serpentine design. Additionally, the power density of bio-inspired fuel cell differed even more, up to 40%, than that of single serpentine fuel cell at the highest current density measured in this study. This was indicative that the bio-inspired design could extend its peak performance range closer to the mass transport region compared to the single serpentine design. In addition to the explanations above, this relative high performance was partly attributed to the lack of a direct connection between the inlet and outlet for the bio-inspired design, which had to force the water through the GDL whereas the single serpentine design had to force the water through long meandering channels. The lack of a direct connection increased the pressure differential between the inlet and outlet that, in turn, increased the average velocity and reactant concentration within the GDL, both of which helped with higher performance. These will be quantified later on with the detailed computational simulations that complemented the present experiments.

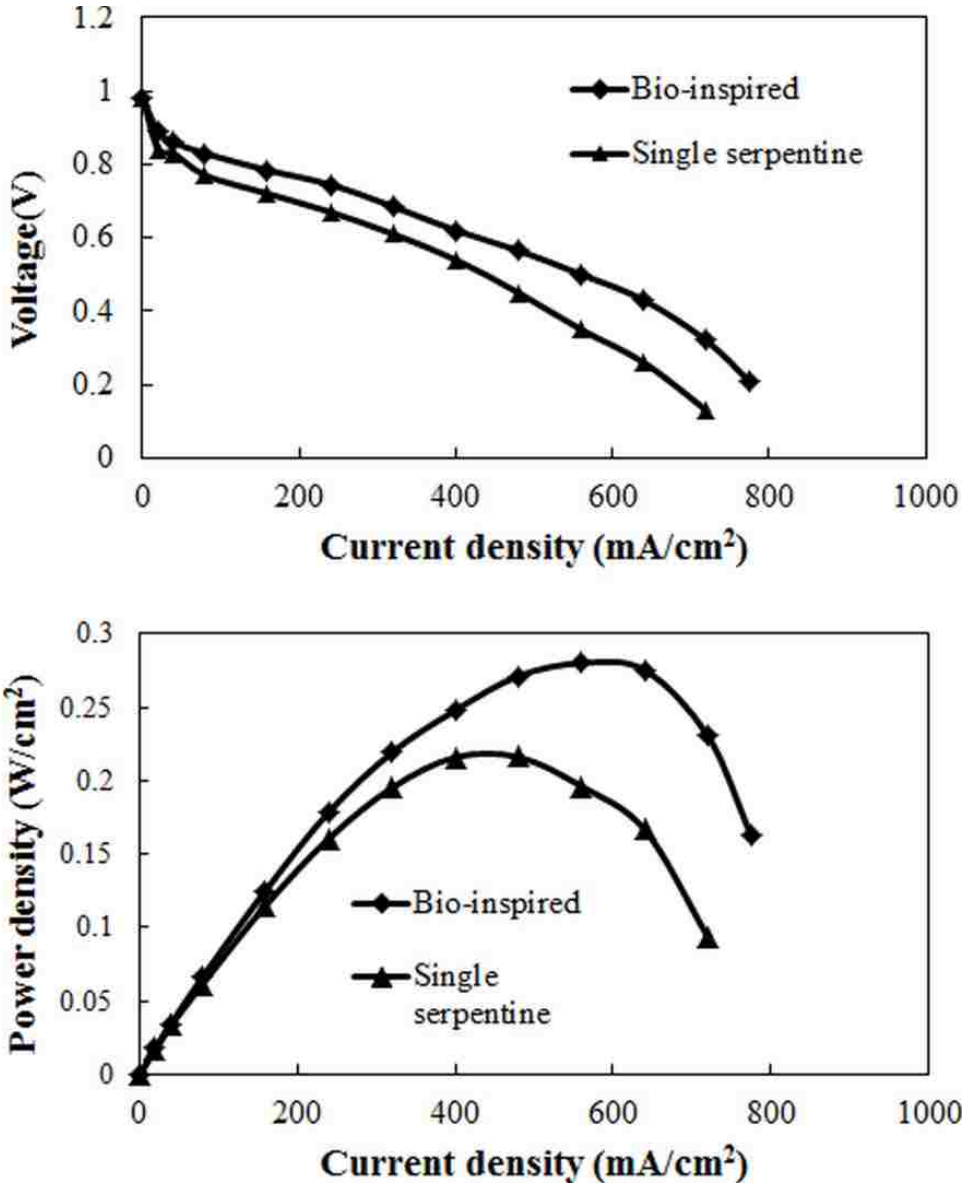

Figure 5.1 Polarization and power curves obtained for experiments

Polarization plot from the simulations suggested superior performance of bio-inspired design against single serpentine design as computations also depicted a trend similar to the experiments as shown in Figure 5.2.

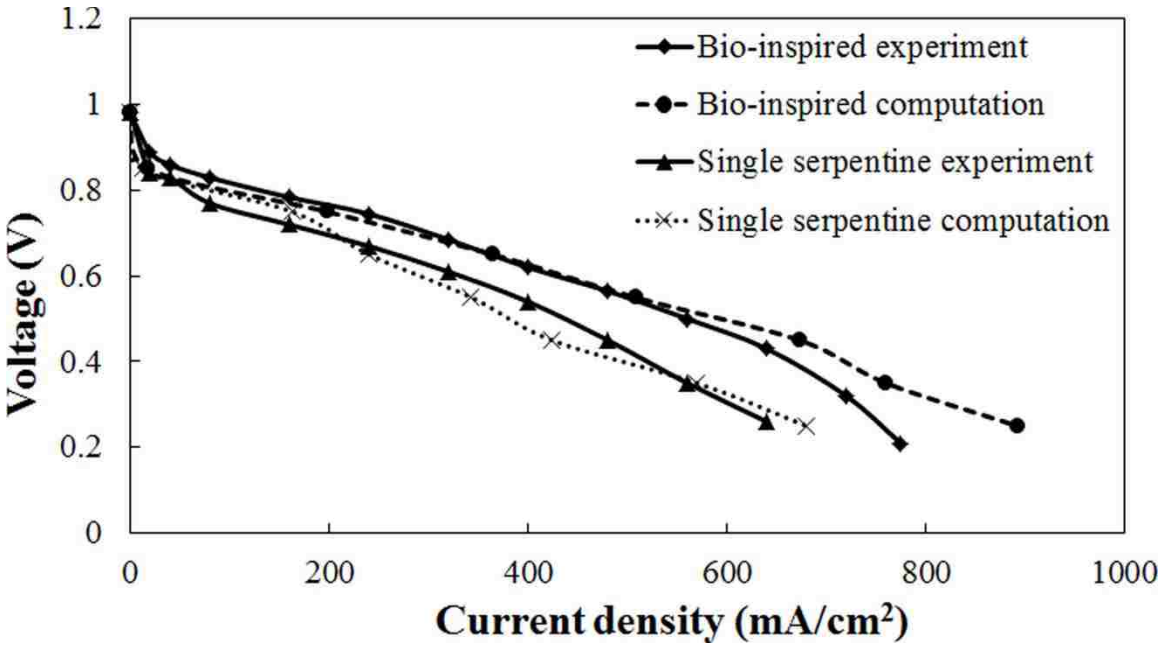

Figure 5.2 Simulation and experimental polarization curves

While the computations agreed well with the experiments for both the bio-inspired and conventional designs, the difference between the experiments and simulations at high current densities was somewhat noticeable (about 10-20%). This was, to a large extent, attributed to the limitations of the software in predicting and simulating the dynamics of the liquid water condensation and multiphase flow effects in the channels. At low current densities, the effects of water were not very pronounced but, at high current densities, as discussed earlier, the mass transport losses increased which were more difficult to accurately model. The difficulty was also partially due to the challenges in accurately predicting the type of flow regimes at a particular flow condition. In addition, it was observed that considerable contact resistances were induced between the GDL and copper plate interfaces due to oxidation, and were, only to an

extent compensated for in the simulations. The effect of current density on contact resistance is two folds: increasing current density increases the temperature of the cell, decreasing the resistance in turn; however, the water production also increases in conjunction with the pressure drop at the cathode, resulting in an unfavorable effect on contact resistance [32].

In the following, the computational results will be presented to complement the above performance experiments so that a complete perspective could be gained in order to explain the observations reported here. Although the simulations were conducted at all conditions considered in the performance curves (various voltages/currents), only the computations at a relatively low voltage of 0.35 V will be discussed in detail below since the bio-inspired flow field performed significantly better relative to its conventional counterpart at conditions in which the concentration losses dominated and therefore the differences were more pronounced. The simulation results for 0.65 V have been presented and discussed in the later sections.

5.2 PRESSURE DISTRIBUTIONS

Pressure distribution within a fuel cell is an important parameter while considering the overall performance. A relatively high pressure differential across the inlet and outlet channels administrates better water management capabilities but induces non-uniform reactant distribution and parasitic losses within the cell. A design that can reduce the water buildup with the least pressure loss is therefore preferred.

Figure 5.3 shows the static pressure across the bio-inspired and single serpentine flow fields on the cathode side GDL's at a voltage of 0.35 V. Note that the scaling of the pressure contours are different as the magnitudes of the extremes of the scale varied substantially.

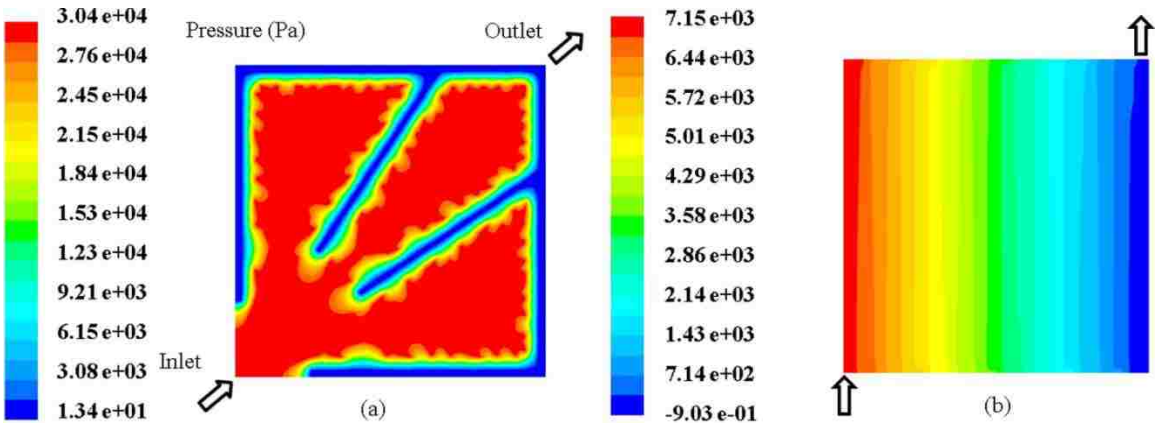

Figure 5.3 Pressure distributions within cathode GDL at 0.35 V (a) bio-inspired (b) single serpentine

Since the inlet and outlet channels of the bio-inspired design were disconnected, it yielded a large pressure drop across the discontinuity. As a result of this pressure differential, the dominating flow was convective transport in the channels of this nature-inspired fuel cell. The pressure differential within the inlet channels was around 600 Pa, which was relatively small. The single serpentine channels, on the other hand, had

considerable pressure drop that was on the order of 700 Pa. This was beneficial for water removal but resulted in large parasitic losses.

5.3 VELOCITY DISTRIBUTIONS

Velocity distribution within a fuel cell determines the reaction rates and water removal capabilities. For reaction rates and water removal rates to be admissible, large to moderate flow velocities are preferred within the fuel cell channels. Low flow velocities may result in membrane flooding especially at low current densities and as a result degrade the membrane life. On the other hand, high velocities may cause incomplete reactions and low residence times for reactants that may also result in membrane dehydration.

Velocity distributions of reactants and products in the GDL are dependent upon flow field design. Figure 5.4 presents the velocity fields at the cathode GDL of the bio-inspired and traditional fuel cells considered here.

Note again that the scales were different due to the velocity variations in both geometries. The velocity magnitudes were on the order of a few tenths of a meter per second in the bio-inspired design in contrast to the velocities on the order of a few millimeters per second in the single serpentine design. The velocities at the ends of the secondary and tertiary channels of the bio-inspired design were much higher compared to the velocity within parent channels. This observation suggested that the liquid water in the GDL was forced through into the outlet channels for promoting better water removal.

The velocity profile in the case of the single serpentine was far more uniform, implying relatively sluggish water removal.

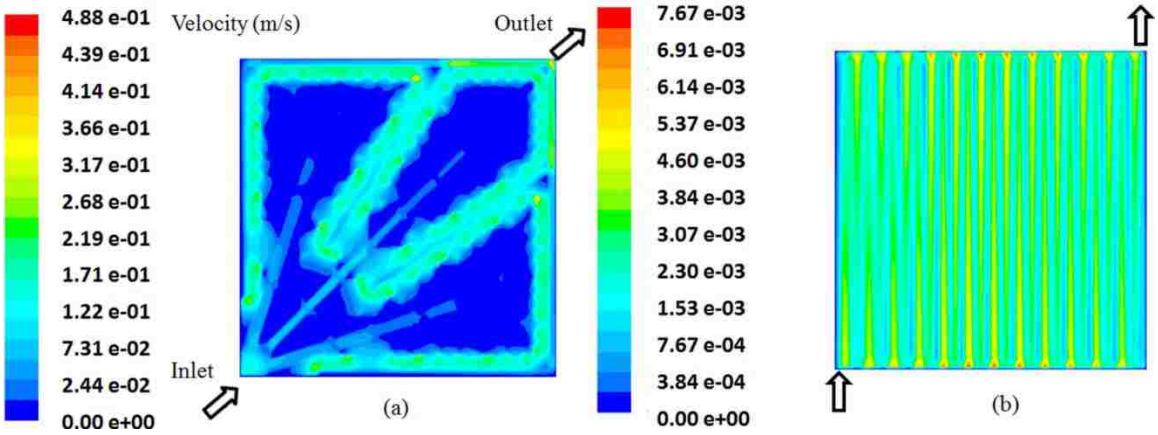

Figure 5.4 Velocity distributions at cathode GDL at 0.35 V (a) bio-inspired (b) single serpentine

5.4 REACTANT MASS DISTRIBUTIONS

Reactant mass fraction distributions tend to follow velocity distributions in a similar manner as uniform reactant densities lead to uniform current density production across the cell. On the other hand, higher reactant mass fractions result in higher reaction rates, which in turn result in higher current densities.

The computations of hydrogen distributions at the anode GDL of the bio-inspired and conventional designs are illustrated in Figure 5.5. For the bio-inspired design, the

area of the GDL below the primary channels had hydrogen mass fractions around 0.165 while the areas below the ribs adjacent to the secondary and tertiary channels were around 0.193.

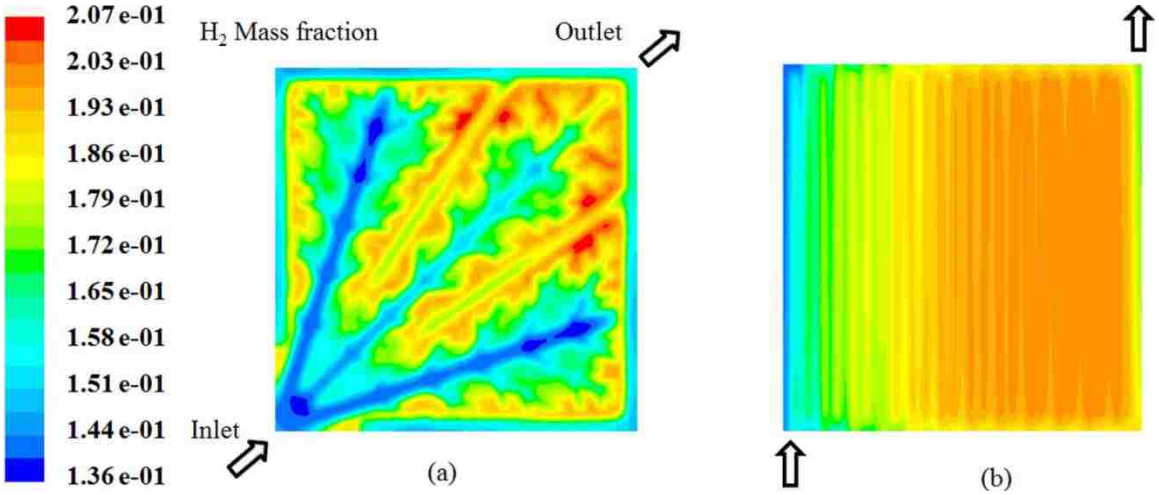

Figure 5.5 Hydrogen distributions at anode GDL at 0.35 V (a) bio-inspired (b) single serpentine

There were some localized regions with hydrogen mass fractions around 0.2 while the rest of the fuel cell including the outlet channels was around 1.72. On the other hand, the hydrogen distribution within the GDL of the single serpentine design did not show such large variation in hydrogen mass fraction compared to the bio-inspired design, that is, reactant concentration was fairly more uniform while a higher hydrogen mass fraction was observed towards the outlet region. The large variation in hydrogen mass fraction in

the bio-inspired design substantiates the cause for higher overall current density across the cell.

The simulations of oxygen distributions at the cathode GDL are shown in Figure 5.6 for both the bio-inspired and single serpentine flow fields.

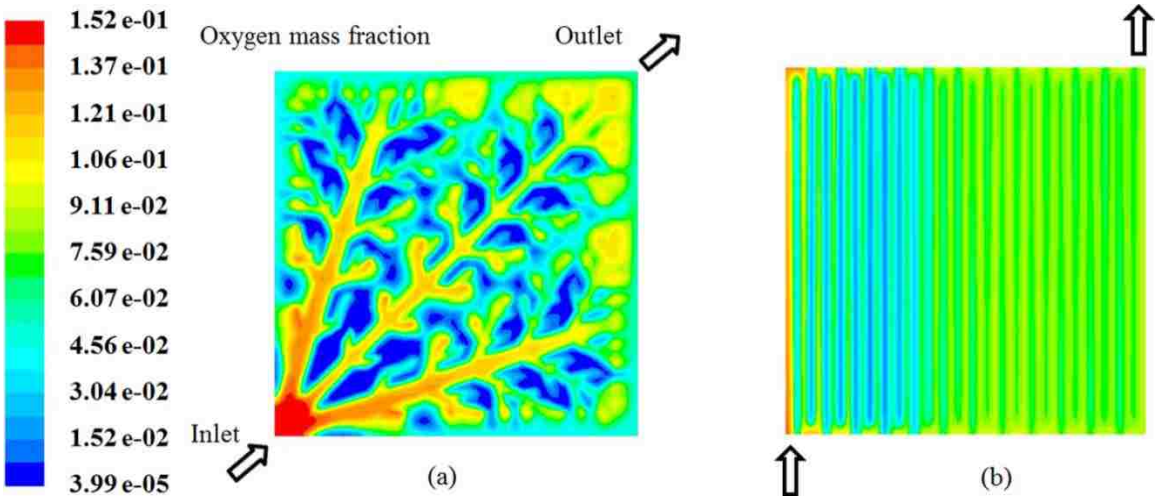

Figure 5.6 Oxygen distributions at cathode GDL at 0.35 V (a) bio-inspired (b) single serpentine

As can be seen, the bio-inspired design was far more non-uniform compared to the hydrogen distribution profile shown in Figure 5.5. Forced convection was the primary transport mechanism due to the pressure differential in addition to the lack of a direct connection. On the other hand, diffusion was the primary transport mechanism in the single serpentine channels. Because diffusion is a relatively slow process, the mass

transport losses at the cathode side were exacerbated at high current densities. Convective flow equalized the pressure differential by driving the products under the land areas to the outlet channels. This was an indication of the higher concentration of oxygen in the GDL that was representative of higher performance. In comparison to hydrogen, oxygen is the limiting factor for reaction rates due to its ionization energy requirements and to ionic transport losses. Hence a design performs better where higher oxygen distribution gradients are seen. In this case, the bio-inspired design clearly showed a large gradient compared to the single serpentine design.

5.5 WATER MASS FRACTIONS IN CHANNELS

Figure 5.7 shows the computed water distributions at the cathode channels for both designs at 0.35 V. The water mass fraction in the channels is representative of the water vapor content in the inlet (humidified) gases and resulting product gases. An indirect correlation can be brought about based on the fact that the vapor is capable of condensing and hence the probability of finding liquid water is high at the places where the vapor mass fraction is high. The inability to dynamically model liquid water is due to the lack of proper software than can combine both the volume of fluid (VOF) and fuel cell module. The VOF model is useful to model liquid water on free surfaces but Fluent does not include the VOF model in the fuel cell model. On the contrary, the present simulations manage to provide saturation model to predict the liquid water in porous media, which has been discussed earlier in the computational methods.

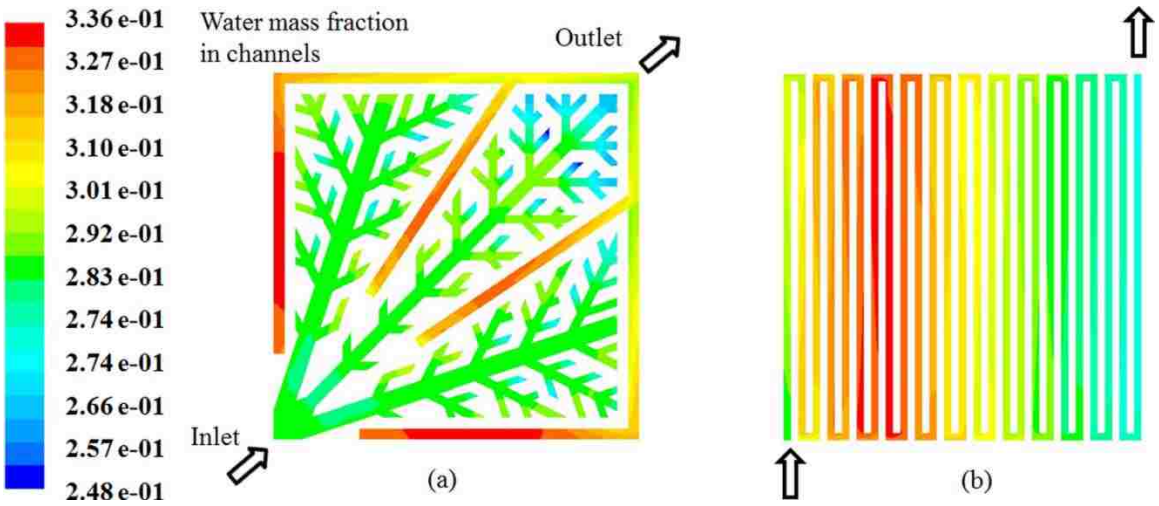

Figure 5.7 Water mass distributions at cathode channels at 0.35 V (a) bio-inspired (b) single serpentine

At relatively high current densities or lower voltages (e.g. 0.35 V), overall water content in the bio-inspired channels was lower compared to the single serpentine design, indicating better water management capabilities of the former design. In particular, the bio-inspired design had lower water content near the inlets and higher water content near the outlets. This was a good outcome as it was suggestive of the fact that more water was evacuated from the inlet channels towards the outlets. The single serpentine channel showed high water content near the inlets compared to the outlets which is clearly a drawback of the design. Although this conventional design was capable of removing water within the channels decently due to pressure differentials, it was at the cost of flow velocities, which were apparent from the velocity distributions at the GDL in Figure 5.4(b).

5.6 WATER SATURATION

Water saturation, which represents the fraction of the GDL pore sites that is filled with liquid water, is critical to the performance of a fuel cell. A pore filled with liquid water is impermeable to any reactant or product gases and hence reduces the number of active sites where gases can penetrate through the catalyst. Thus, a design which can prevent pore saturation to a large extent is preferred. It is to be noted that the nature of the GDL is also a critical player in this regard, which has been discussed in detail later on. Figure 5.8 illustrates the water saturation at the GDL of the cathode of the bio-inspired and single serpentine channels from the detailed computations.

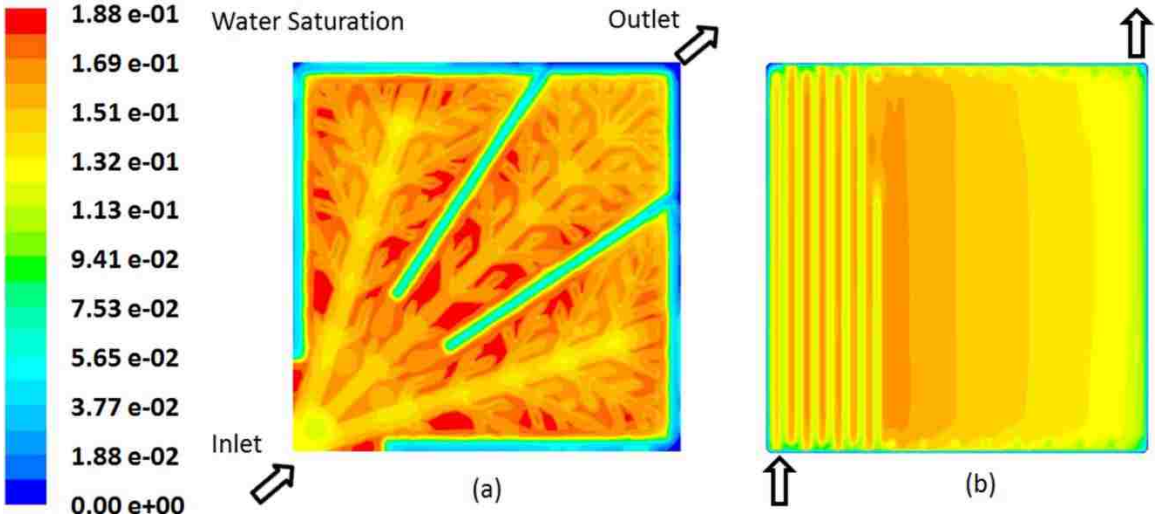

Figure 5.8 Water saturation at cathode GDL at 0.35 V (a) bio-inspired (b) single serpentine

The bio-inspired design showed higher water saturation below the land areas and lower saturation under the channels. This was expected from an interdigitated design as the water was forced through the GDL to the outlets. In addition, the proximity of the outlet channels to the ends of the inlet channels gave an opportunity for the water to enter the outlet channels well before reaching the end of the inlet primary channels, enhancing the water removal capability of this geometry. The single serpentine design showed fairly high water saturation within the GDL closer to the inlet. This meant that a large fraction of the pores closer to the inlet were clogged with liquid water, interrupting the flux of reactant gases towards the catalyst resulting in low reaction densities. These computations of water distributions within the channels of both fuel cell types will be supplemented below with direct visual observations using the transparent bipolar plates.

5.7 COMPARISON OF SIMULATIONS

As mentioned earlier, the simulations were conducted at all voltages but the results at 0.35 V have been discussed in detail. The simulations at 0.65 V have been presented in comparison to the results at 0.35 V in Figure 5.9. The water saturation in the cathode GDL has been presented in Figure 5.9(a) and (b). It can be observed that the GDL at 0.65 V is uniformly saturated at an approximate value of 0.132. The GDL at 0.35 V showed higher water saturation which was indicative of the liquid water content at this voltage. In addition, since the bio-inspired design showed a substantial performance improvement at 0.35 V compared to 0.65 V, it was meaningful to study the results at 0.35 V in more detail.

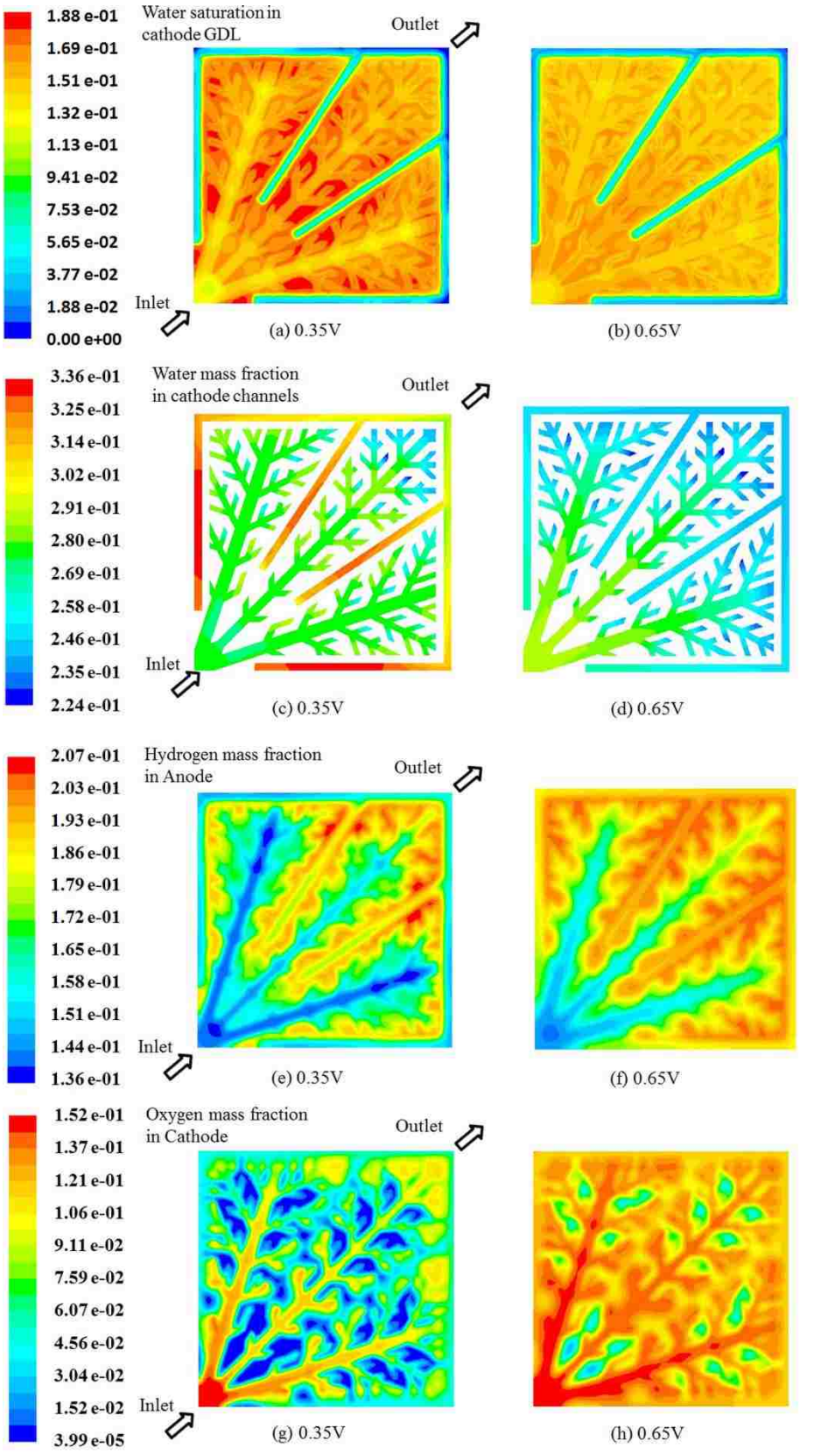

Figure 5.9 Comparison of simulation results for 0.35 V and 0.65 V

Figure 5.9(c) and (d) illustrate the water content in the cathode channels. The water content was much lower in the outlet channels whereas the outlet channels at 0.35 V showed a far greater increase in water content. The hydrogen and oxygen species distributions at the GDL are displayed in Figure 5.9(e-h). Clearly the consumption at 0.65 V was lower resulting in high mass fractions throughout the GDL surface. Also it is a known fact that the oxygen reaction rate is the limiting factor in a fuel cell electrochemical reaction. At 0.65 V, the fuel cell was unable to consume the oxygen efficiently which resulted in a very uniform oxygen distribution profile. On the other hand, the profile at 0.35 V was much more non-uniform indicating a good consumption rate

Also, higher consumption of species relates to higher GDL water saturation and channel water contents which are acknowledged by Figure 5.9(a) and (c). Thus it could be concluded from the above illustration, that the study of the fuel cell species profiles at low or medium current densities made little sense when the objective was to improve the water management capabilities of a fuel cell by optimizing the flow field design. In this case, the bio-inspired design clearly showed substantial performance improvement at higher current densities for which an appropriate analysis of experiments was conducted in the sections that follow.

5.8 EXPERIMENTAL OPTICAL IMAGES

Optical images of water distribution within the channels are a means of understanding the complex fluid dynamics within micro channels. The flow fields of

PEM fuel cells consist of channels with hydraulic diameters smaller than 2 mm and hence can be classified as micro channels. Table 4.3 gives more information on the hydraulic diameter of the individual branches of the bio-inspired design. The channel geometry parameters influence the flow patterns observed that have been discussed in the following sections.

5.8.1 Flow Patterns. In such small channels, the surface area per unit volume is relatively high which implies that surface tension, cohesive and viscous forces are dominant forces. Gravitational forces are minor and in most cases could be neglected. Dimensionless parameters such as the Weber number and Reynolds number can be used to determine the characteristics of the flow when gravitational effects are low. The Weber (*We*) number and Reynolds (*Re*) number are represented by equations (24) and (25) below.

$$We = \frac{\rho V^2 L}{\sigma} \tag{24}$$

$$Re = \frac{\rho V L}{\mu} \tag{25}$$

Here, ρ is the density difference between phases (kg/m^3), g is the acceleration due to gravity (m/s^2), L is the characteristic length (m), V is the characteristic velocity of the flow (m/s), σ is the surface tension (N/m), and μ is the dynamic viscosity (kg/m-s).

The gravitational force can be neglected in micro channels as a result of which the surface tension, inertial and viscous forces are critical. Reynolds number is the ratio of inertial forces to viscous forces. It determines whether the flow is laminar or turbulent. In most fuel cells, the flow is laminar with a *Re* number less than 500. At very low flow velocities (*Re* = 40), a pure slug was observed whereas when the velocity increased slightly (*Re* = 200) a transitional flow from a slug to annular with an extended boundary was observed. If the velocity is increased further (*Re* = 400), annular regime with core gas flow was observed [33]. Weber number represents the ratio of inertial and surface tension forces. This number is useful in determining the type of flow patterns in the absence of gravity annular flows are seen in the region where inertial forces dominate (*We* > 2), slug and bubbly flows are observed in regions where surface tension forces dominate (*We* < 2) [34].

Based on the above understanding, it may be concluded that of the many flow patterns, bubbly, slug and annular (film) flows are the most commonly observed flow regimes in fuel cells. The combination of one or more of the above three flow regimes is termed as transitional flow. In addition, the identification of flow patterns gets more complicated due to the effect of various operating conditions, including humidity levels, temperatures, flow field designs, and different surface materials (GDL and channel) [33].

It should be mentioned that copper and Lexan are hydrophilic in nature with contact angles in the range of 78^0 while the GDL carbon cloth used is hydrophilic in nature. In the present study, a carbon cloth with 30% of the micro-porous layer (MPL) is PTFE coated. PTFE increases the hydrophobicity of the fibers that helps the growth and detachment of water from the GDL pores. It is to be noted that the flow regimes are very

much dependent on the type of GDL used; for example, water droplets on carbon GDLs are circular in shape and do not spread out laterally over the surface. Some of the commonly observed flow regimes are visually demonstrated in Figure 5.10 below.

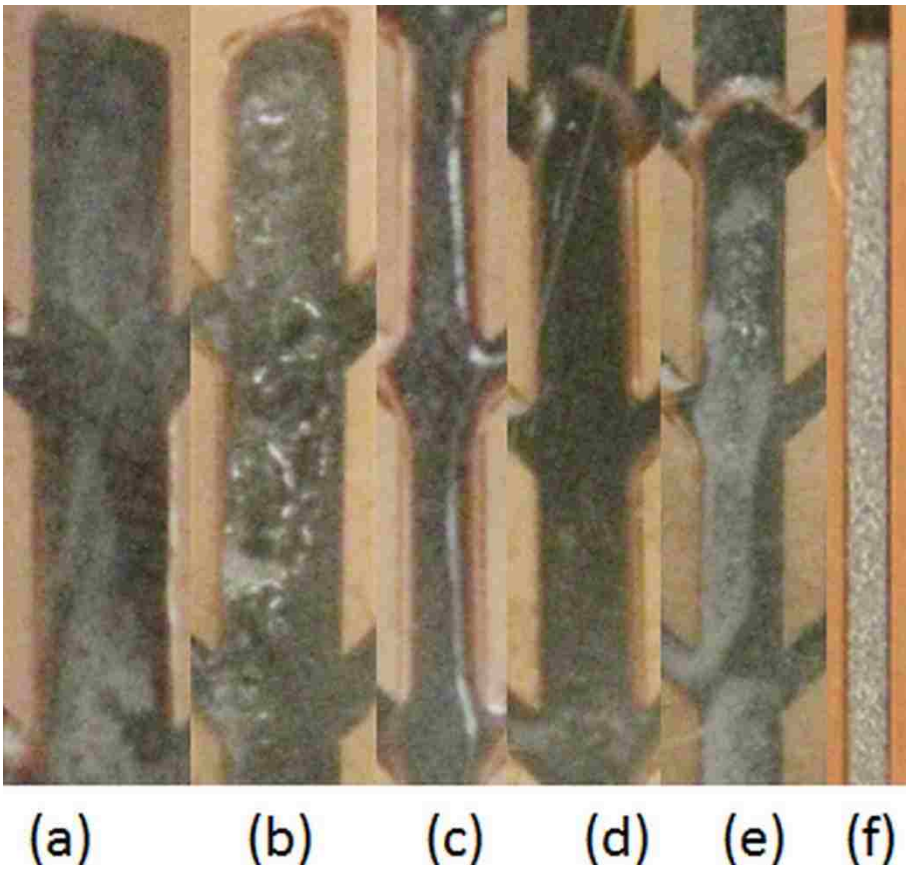

Figure 5.10 Flow patterns (a) mist (b) bubbly (c) film (d) stable slug (e) unstable slug (f) plug

Mist flow (Figure 5.10a) is identified as a single-phase flow, in which the vapor is about to condense on the channel walls. It consists of partially humidified gas and some

stray water droplets may be seen but they evaporate due to the flowing air stream. The second type of flow is bubbly flow (Figure 5.10b) which consists of water droplets emerging from the GDL surface. The droplets remain adhered to the GDL surface with strong surface tension forces until they coalesce into oncoming columns of water or evaporate into the flow of air. The water emerging from the GDL adds to the water content in the channels that increases the tendency of the humidified air to condense and form slugs. A true bubbly flow may not be possible in fuel cells due to the low flow velocities but a transitional flow with large number of bubbles is plausible. The next regime is a film flow (Figure 5.10c) in which liquid water adheres to the boundaries of the channel walls due to high surface tension forces at the hydrophilic surfaces. The film forms when the influx of water from the GDL is sufficiently high, causing the water droplets to coalesce and get wicked into the walls, resulting in a film or boundary flow [35]. The shear forces that act on the film due to the flowing gases have little effect. The hydrophilic surfaces (channel walls) may hold more water in the form of films; it distributes water more uniformly [19]. When the water content in the channels keeps increasing due to higher water production, the film continues to grow and accumulates into a sluggish block of water called a slug as shown in Figure 5.10(d). In this case, since the flow rate is kept constant and the current density is increased, it would mean that with the increase in water production, the local velocity of air decreases and hence favors slug formation compared to stratified flows or wavy flows. The difference between slug flow and bubbly flow is the presence of air. Slug flows are columns of water flowing below the air stream mostly along the GDL surface while bubbly flow contains a large number of air bubbles dispersed in liquid water. When the reaction densities increase further

mostly in the high current density regions, an unstable slug flow can be formed. It is a flow regime in which the water droplets are released into the slug flow from the surface of the GDL, hence causing a large number of water droplets clustered together and flowing along with the slug as shown in Figure 5.10(e). Plug flows on the other hand are large liquid columns with some entrapped gases within, as illustrated in Figure 5.10(f). The difference between plugs and slugs is the position of the liquid column. Slugs are located close to the GDL and are very slow moving. Plugs are mostly localized to the channel depth region and do not slide over the GDL like slugs. Also, as will be discussed in detail later on, plugs were seen in the single serpentine channels while they were absent to a large extent in the primary channels of the bio-inspired design. The reason is explained in detail in Figure 5.11. A slug to plug transition has been displayed in the illustration of the flow pattern differences, which gives a better understanding of the difference. Plugs completely block the gas flow and hence build large pressure differentials behind, which help force them through the channel lengths. Slugs allow gases to flow over them giving lesser resistance to flow compared to plugs.

In addition to the knowledge of flow patterns, understanding the forces arising due to surface tension, capillary and under-rib flows is also important. As illustrated in Figure 5.11, single serpentine channels have minimal under-rib flows as a result of which the downward forces generated due to the suction effects of under-rib flow are weak. Consequently the capillary effects dominate due to the small channel width (1 mm) and hence the water level rises.

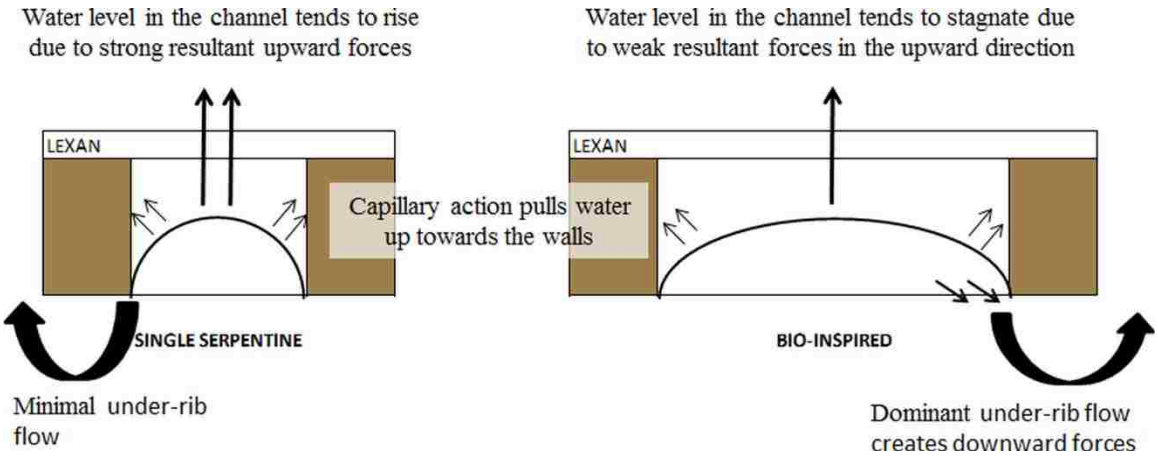

Figure 5.11 Schematic of resultant forces in single serpentine and bio-inspired design channels

This is proof of the fact that single serpentine channels showed plug formations in addition to slugs. On the other hand, in the bio-inspired design, the under-rib flow phenomenon is dominant due to the interdigitated design and hence strong downward forces due to the suction effect of under-rib flow cancels out a major portion of the capillary effects. It is also to be noted that the bio-inspired primary channels were 2.5 mm wide that resulted in weaker capillary effects in comparison to 1 mm channels. Accordingly, the water does not rise as much along the depth of the channel, minimizing the possibility of plug flow formations in bio-inspired channels. The optical image obtained from direct visualization of fuel cell channels supports this explanation. It is to be noted that the water that appears on the surface of Lexan is much more visible to the naked eye compared to slugs that are below the Lexan surface closer to the GDL.

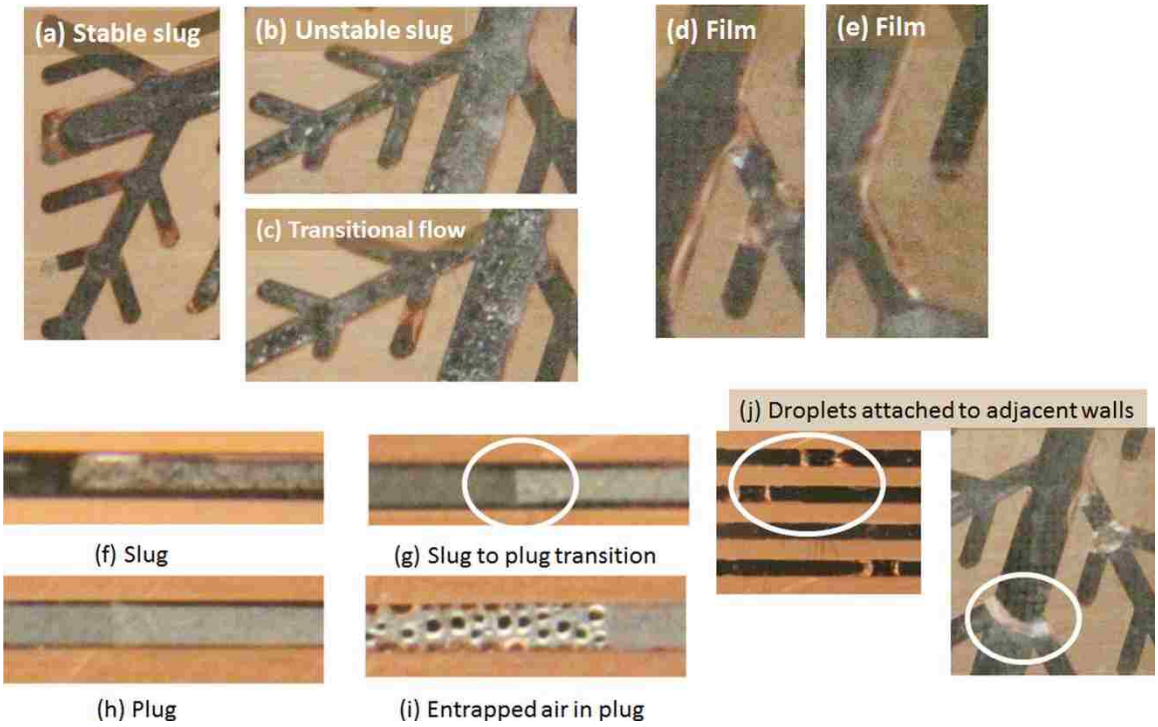

Figure 5.12 Illustration of flow patterns from single serpentine and bio-inspired channels

Figure 5.12 (a, b, f–i) presents more information on the identification of plugs and slugs. The images lettered from (a) to (e) belong to the bio-inspired channels, (f) to (i) pertain to single serpentine channels and (j) has two parts of which the left image belongs to single serpentine and the right belongs to bio-inspired channel. The Figure 5.12 intends to illustrate the variations of the flow patterns under the same regimes. For example, the slugs (a), (b) and (f) are substantially different from one another regardless of being in the slug flow regime. This gives evidence of how remarkable the role of geometry shape and dimensions play in the resulting flow pattern. Image (f) displays a slug in the single serpentine channel. It is clear that the slug is close to the GDL surface while the plug in (h) is close to the Lexan surface. A transition between slug and plug has been shown in

image (g). The variation in depth is clearly indicated by the transition. From the earlier discussion, it was clear that plugs could contain large quantities of entrapped gas bubbles, which are illustrated in image (i). In the case of the bio-inspired design, slugs were displayed but the transitional flow in (c) is of particular interest. It was earlier argued that true bubbly flows might not be seen in fuel cells due to the low flow velocities. But the image displays large number of bubbles. It is also to be noted that those bubbles were dispersed in a sheet of liquid water. Thus it is an intermediary between slug flows and pure bubbly flows. Figure 5.12(d) and (e) show two films that were very different from each other. Both films were attached to the wall but (d) shows a film in the primary channel that was attached to some condensed liquid water in the secondary channels while the film in (e) extended along the boundary of the wall from the primary to the secondary channels. Mist was also seen along the film. This indicates that the flow phenomena that occur downstream have a substantial effect on the flow patterns upstream. Figure 5.12(j) is illustrative of droplet formations in the channels. The droplets in both designs were quite similar except for the fact that the channel dimensions were very different. The droplet size in the single serpentine channel was small and thin while the droplet in the bio-inspired design was large and thick. This suggested that a large bubble is required to form in the bio-inspired design otherwise it would result in film flows. But in the single serpentine, droplets were far easier to form due to the proximity of the adjacent walls (1 mm width compared to 2.5 mm width in the bio-inspired primary channels).

5.8.2 Performance and Stability. Experiments were conducted to visually observe the water formation and movement dynamics within the channels of the bio-inspired and single serpentine fuel cells using the transparent end plates. The flow rates of hydrogen and air were maintained at 300 ml/min and 1000 ml/min, respectively, for all of the experiments. This corresponded to a stoichiometry of 2.0 at anode and 3.0 at cathode for a current density of 1000 mA/cm^2. These flow rates were ensured so that at no point of operation should the fuel cell encounter insufficient reaction flow rates. It is known that the reactant consumption is voracious and there is a possibility of reactant starvation at high current densities. In case this occurs, the water produced in starvation mode would be incorrect and according, the fuel cell must operate in an environment where the reactants are slightly in excess for accurate experimental observations.

The optical images of the operating fuel cell channels were recorded at three different voltages. The two-phase flow patterns in the bio-inspired flow fields were compared to the same in the single serpentine geometry as shown in Figure 5.13. Also note that the numbering of the primary channels will be referred to as first, second and third primary channels. The voltage vs time plots shown in Figure 5.14 are indications of the stability of the flow field at various levels of the fuel cell operating range. The three voltages were picked from the polarization plot, designating the different regions of activation losses, ohmic losses, and mass transport losses.

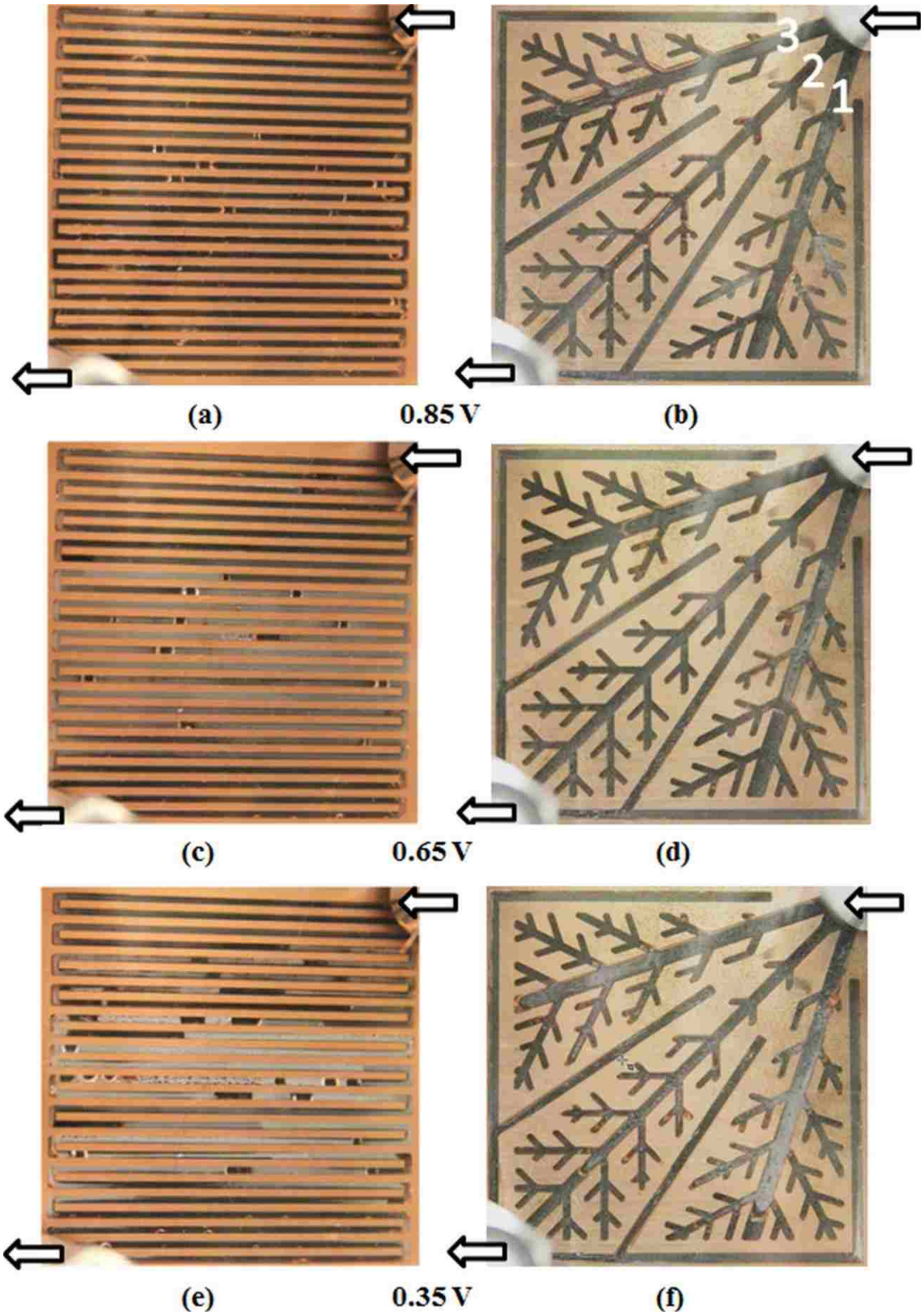

Figure 5.13 Optical images of water distribution at three different voltage levels

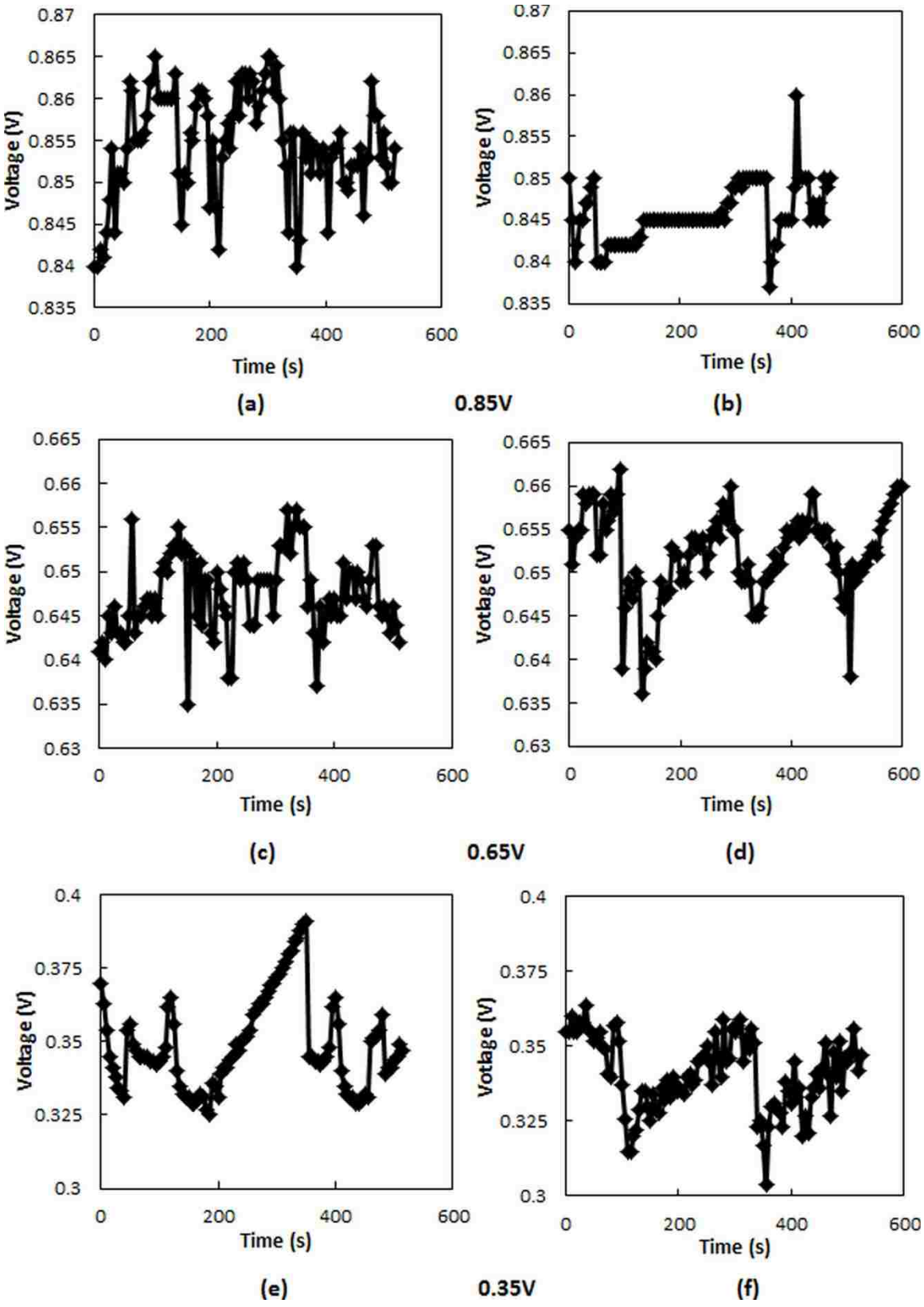

Figure 5.14 Voltage vs time plots for single serpentine and bio-inspired design at three different fuel cell voltages

In the activation loss region, the current density is low and the voltage is high because the reactions are sluggish as they are overcoming the activation barriers. Hence, low water content was observed at low current densities. The water presented itself as mist flows and transitional flows at low current densities/ high voltages (Figure 5.13(a) and (b)). Small slugs were also observed but limited to certain regions of the fuel cell generally towards the ends of the primary channels. It is expected that the water formation is not uniform throughout the GDL and presents itself in selective regions, mostly towards the middle and end of the fuel cell channels. In the single serpentine channels, small droplets could be seen adhering to the walls near the inlet. This phenomenon is due to the fact that surface tension effects dominate and hence form droplets which adhere to the walls with adhesive forces. Further down the channels, menisci of liquid water could be seen to adhere to adjacent walls, restricting the flow passage. Near the middle of the fuel cell, where water content was high due to higher reaction densities some air gaps were present between columns of liquid water (slugs). The formation and expulsion of slugs are associated with voltage fluctuations. Since the slug formation was limited in low current density operation, the voltage fluctuations were expected to be small. This was supported by a 25 mV variation in voltage shown in Figure 5.14(a). The bio-inspired design showed a slightly similar trend with small slug formations, which were located near the middle of the fuel cell, mainly in the third primary channel. The second primary channel displayed films and mist flows. The first primary channel predominantly showed mist flow and some slugs on its branches. The voltage for the bio-inspired design was comparatively more stable than the single serpentine with a 15 mV variation shown in Figure 5.14(b). This could be attributed to

the slug formation and expulsion. Mist flow and film flows caused little voltage fluctuations as they posed little resistance to the gas flows.

The second region on the polarization curve is the ohmic loss region, which is also known as the charge transport region. A significant voltage magnitude is expended to drive the conductive charge through the fuel cell. In this region, reactions have sufficient energy to overcome the activation barrier hence increasing the fuel cell temperature as well as introducing considerable amount of water into the channels. Most of the resistances observed in this region are due to the electrolyte. Resistances posed by the GDL and contact resistances between the GDL and channel surfaces also emerge as significant losses in this region.

The single serpentine channels showed significant liquid water from the middle to the third quarter length of the channels. The water content was significantly higher, showing larger slug formations in the fuel cell. The slugs were long with entrapped gas pockets in between adjacent slugs. The voltage variation was similar to the behavior at 0.85 V with a typical 20 mV fluctuation as displayed in Figure 5.14(c). Similarly, the bio-inspired design showed significant slug formation in all three primary channels. It could also be spotted from the images that the slugs showed a good number of water droplets emerging from the GDL surface that accumulated at the bottom of the slug. This indicated the amount of liquid water being formed over the GDL surface was considerable in comparison to the operating condition at 0.85 V. The regions of water formation were also concentrated towards the middle of the fuel cell. At the intersection of the primary and secondary channels, the slug divided and the movement of water along the secondary channels was slightly speeded up due to the capillary and surface

tension effects of the thin channels. Figure 5.14(d) shows a 30 mV fluctuation which was supportive of the fact that the GDL was dealing with larger quantities of water. Additionally, the fluid was forced through the GDL into the outlets since the inlet and outlets were not directly connected in the bio-inspired flow channels. This caused relatively larger voltage fluctuations. When the water was removed and the GDL pores were clear of liquid water, the voltage spiked upwards and then decreased again with the accumulation of water both in the channels and GDL.

The third and final region is the mass transport region. This region is critical to a fuel cell's performance as the reactants are consumed voraciously and the electrodes and porous layers have to deal with large water quantities that enhance the difficulties of sustained operation of fuel cells in this region. The liquid water clogs the channels and causes reactant depletion. The presence of liquid water induces higher contact resistances between the GDL and channel interfaces as discussed earlier. Presence of hydrogen and oxygen together is far more detrimental to the life of copper as it corrodes faster subsequently increasing the losses at the current collection zones.

The single serpentine design displayed clogged channels. Figure 5.14(e) showed an 80 mV fluctuation in voltage compared to a 60 mV fluctuation in the case of bio-inspired channels, represented by Figure 5.14(f). The larger fluctuation in the conventional design can be attributed to the presence of plugs while the absence of large plugs in the bio-inspired design resulted in a slightly smaller fluctuation. The bio-inspired channels indicated increased water content in the channels compared to 0.65 V. In-spite of the presence of large quantities of water, there were many secondary channels free form liquid water that allowed for gas diffusion. This also gave more room for the slugs

to penetrate, in addition to the under-rib flow mechanism, resulting in a reduction of water content in the main channels. The secondary channels, owing to their smaller size had higher capillary effects. This caused the water in the main channels to be sucked into the secondary channels. Also this phenomenon resulted in some plug formations within the secondary channels which are seen in the time-sequenced images of the bio-inspired design. Apart from that, slugs were the major flow regimes observed at this voltage. The relatively smaller voltage fluctuations compared to the single serpentine channels suggested that the bio-inspired design was able to perform steadily even at high current densities.

5.9 ROLE OF GDL

Liquid water is transported through the GDL, mainly through the largest pores. The requirement for liquid water to move out is the exit pore of the GDL must be larger than the entry pore and the pores must be larger than the critical radius of the droplet. Small pores cannot transport water due their size being smaller than the critical radius and inhibiting the penetration of water. Water formed at the electrolyte/electrode interface requires sufficient pressure to build up to force the liquid water into the GDL pores. For this purpose, the membrane absorbs water and swells up generating sufficient pressure to push water into the pores [36]. Based on this phenomenon, all the liquid water was forced into the channels in the case of the single serpentine channels but, in the bio-inspired design, the pressure buildup pushed liquid water through into the inlet channels and partly into the outlet channels as well. The lower pressure in the outlet increased the

pressure differential between the electrolyte and the channel and therefore aided in water removal.

In addition to the pore effects, the hydrophilic nature of the GDL also plays a major role in water transport through its pores. Carbon fibers are hydrophilic by nature. To aid the removal of water from the surface of the GDL, the top layer also called as the micro porous layer (MPL), is PTFE coated. This increases the hydrophobic nature of the GDL that aids in the detachment of water droplets from the surface of the GDL. In our case, a carbon cloth GDL with 30% of the MPL coated with PTFE was used. It is expected that the surface of the GDL that is in contact with the current collectors is subject to some damage on compression. The amount of compression determines the extent of the damage.

When the fuel cell is compressed to provide an air-tight seal, the carbon cloth GDL acts as a cushion between the membrane and current collector. Accordingly the GDL deforms and the areas under the lands get compressed while the areas under the channels rise slightly because the channels are void of any material. The carbon fibers tear as a result of the compression.

Figure 5.15 shows the microscopic images of the GDL both before compression and after compression, at a magnification of 250 times. Images in the insets were taken at 500 times magnification with a 60 μm scale. A HIROX KH-8700 optical digital microscope was used to observe the GDL carbon fiber structure.

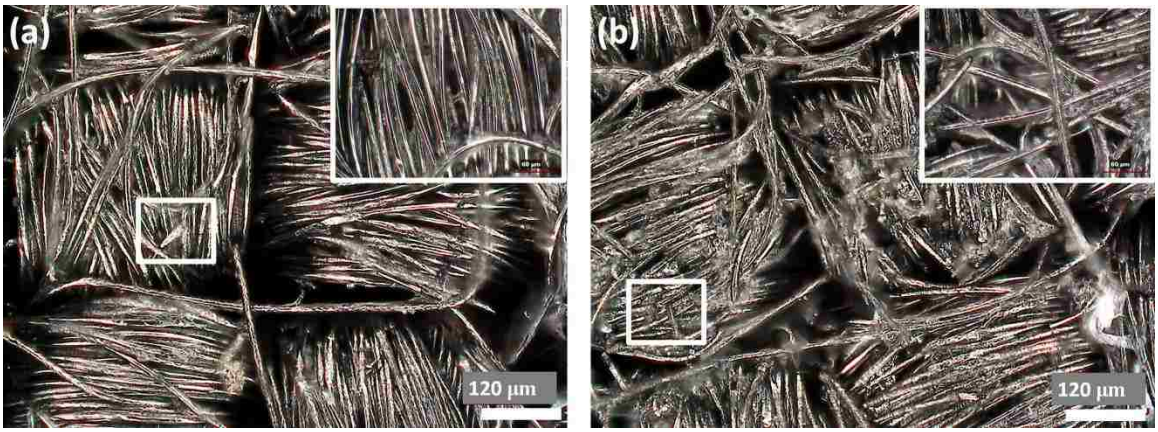

Figure 5.15 Microscopic images of GDL (a) before compression (b) after compression.

A maximum scale size of 30 µm was achieved but the image quality was compromised due to the non-uniform surface topology of the GDL after compression. 3D multi-focus images were obtained using the inbuilt image processing software. The focus was maintained on a bunch of fibers and the layers below and above those fibers was also stitched into one image constituting a multi-focus image. The inset images were built up using 200 layers spaced 2 µm apart along the vertical axis. For higher resolutions and more detailed inspection of fiber, Scanning Electron Microscope (SEM) can be used, but in this case, the images obtained with the optical microscope were sufficient.

The carbon cloth GDL before compression shows fibers wound with few defects. The inset in Figure 5.15(a) shows a magnified image of the fibers with no delamination of PTFE being visible. On the other hand, the fibers in Figure 5.15(b) indicated considerable damage. It could be seen that the organized structure of the GDL fibers on the top layers are lost. Some blurred regions were also observed because of the de-laminated PTFE, which reflected the incident LED light from the microscope differently

compared to the fibers. In the inset of Figure 5.15(b), de-laminated PTFE could be seen between individual fibers. The displacement of the fibers from their normal positions has opened up some gaps which were considerably large. This increased the number of pores available for water transport. In addition, the hydrophobic de-laminated fibers expose the uncoated hydrophilic fibers below that created preferential pathways for water transport [37]. This de-lamination was more pronounced below the land areas. In the case of the bio-inspired design, de-lamination worked in favor because it increased the tendency of water to penetrate into the GDL under the land areas. This was necessary for the water to reach the outlets in an interdigitated design. The advantage was indirectly seen in the time-sequenced images for the bio-inspired design in Figure 5.16.

5.10 TIME-SEQUENCED IMAGES

Images were taken at various time intervals as shown in Figure 5.16 and Figure 5.17. For the bio-inspired design (Figure 5.16), the water removal mechanism was relatively complex. Water removal process began with a swelling droplet as shown in image (b) after which it could be seen that the length of the slugs receded as shown in image (c). The receding slug seemed to push itself into the secondary channels. Image (d) shows the third primary channel with partially cleared channels after which the image (e) shows an increase in slug lengths again. This is due to the large reaction density at 0.35 V. Image (f) displays the first primary channel clear of liquid water with a small residual slug. The removal was apparently a bidirectional process, as suggested by these images.

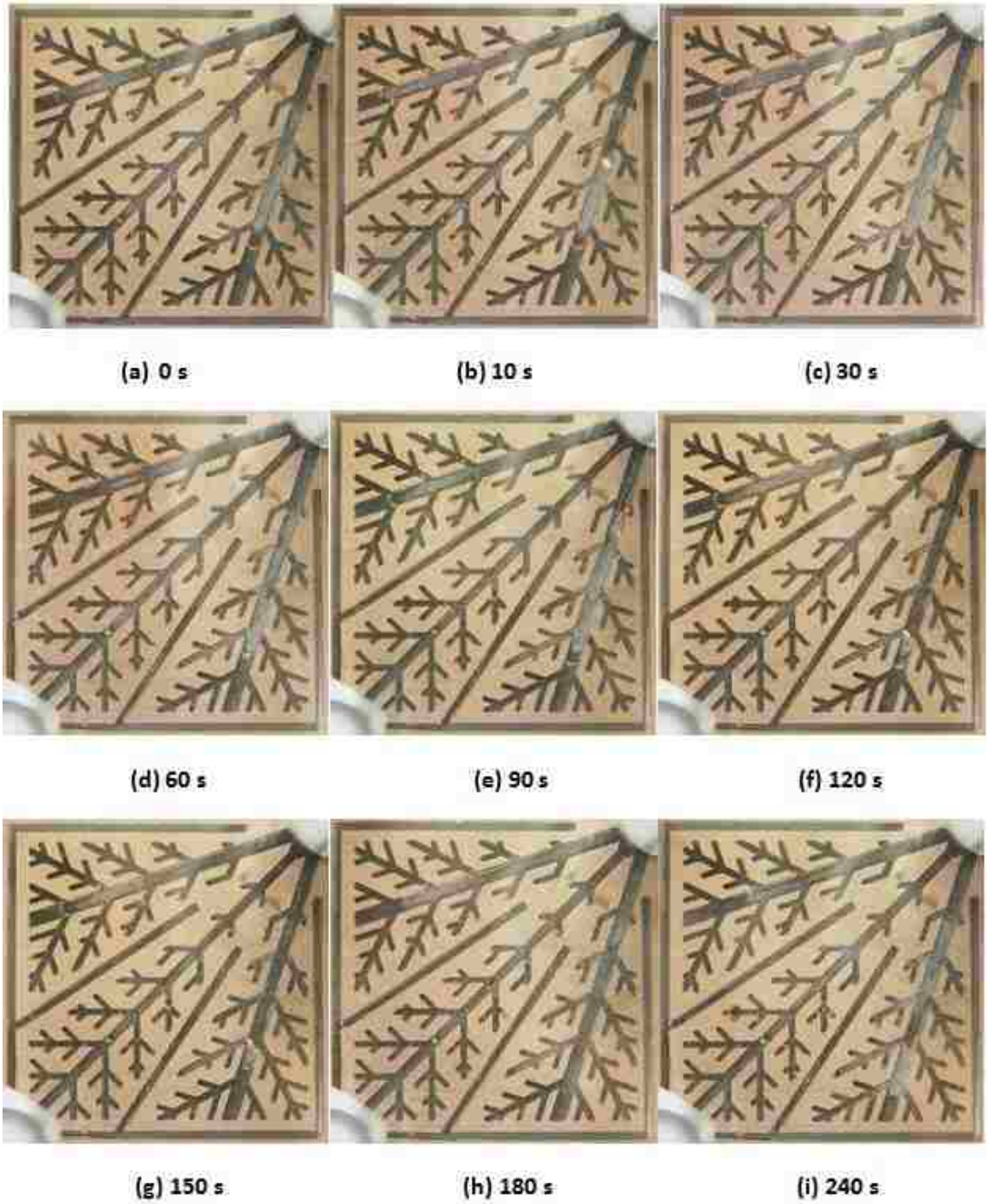

Figure 5.16 Time sequenced images showing water removal in bio-inspired channels at 0.35 V

The slug length receded and the water upstream pushed itself downwards, resulting in a small residual slug in the first primary channel. The same process reoccurred in the third primary channel between (f) and (g). The size of the slug in the first primary channel in image (g) was smaller than the size of the slug in (f). In image (h), the first primary channel was completely clear of water with some mist formation occurring. The third primary channel again filled up with water between (g) and (f). Image (i) shows the reformation of large slugs in all the channels. The second primary channel showed increase in water content throughout the 240 s interval. This is due to the smaller width of the channel (1.8 mm) compared to the first and third primary channels as a result of which the capillary effects and surface tension forces are stronger. In addition, the flow in the second primary channel was much more sluggish in comparison to the flow in the other two primary channels. Thus the performance of this channel somewhat resembles the performance of the single serpentine channels where channel clogging was present. The second primary channel took a further 120 s to remove the water. Subsequently, water quickly accumulated in the second primary channel. Unlike the first and third primary channel where the time interval in which the channels were free from liquid water accumulation, the second primary channel was clear only for a very small time interval. This is expected due to the relatively higher water production rate at this condition. However, the convective transport under the lands compensated for the adverse effects of higher water content in the channels [23].

The single serpentine design had very large quantities of water in the form of plugs at 0 s (beginning of the imaging sequence at 0.35 V) as shown in Figure 5.17(a). After 30 s in (b), the water profile did not seem to change much except for some additional water collection in the channels downstream towards the outlet. In (c), it was observed that the plugs upstream moved downstream resulting in cleaner channels between the inlet and the middle of the fuel cell. Image (d) showed a continuation of the downstream movement of the plugs which were previously present at the middle of the fuel cell in (c). In the middle of the fuel cell in (d), a channel is seen completely void of any liquid water. This was indicative of the plugs being forced out due to large built up pressure differentials across the plug lengths. In image (e), this conventional fuel cell seemed to have filled up with water again showing large number of plugs, this time starting very close to the inlet. Image (f) showed lower water content compared to (e) although the water profile was visually identical. Image (g) was illustrative of a much cleaner fuel cell with relatively lower water content and the absence of dense plugs. Image (h) and (i) demonstrated the reformation of water and the process of water removal was repetitive. It was observed that the middle of the fuel cell in the single serpentine design showed very sluggish water movement patterns. The plugs seemed to have stagnated and took a very long time to move downstream. A similar observation was also made in the middle of the second primary channel of the bio-inspired design. This could be due to overwhelming gas consumption rates at the center of the fuel cell active surface area as a result of which the fuel cells had significant issues handling the influx of water.

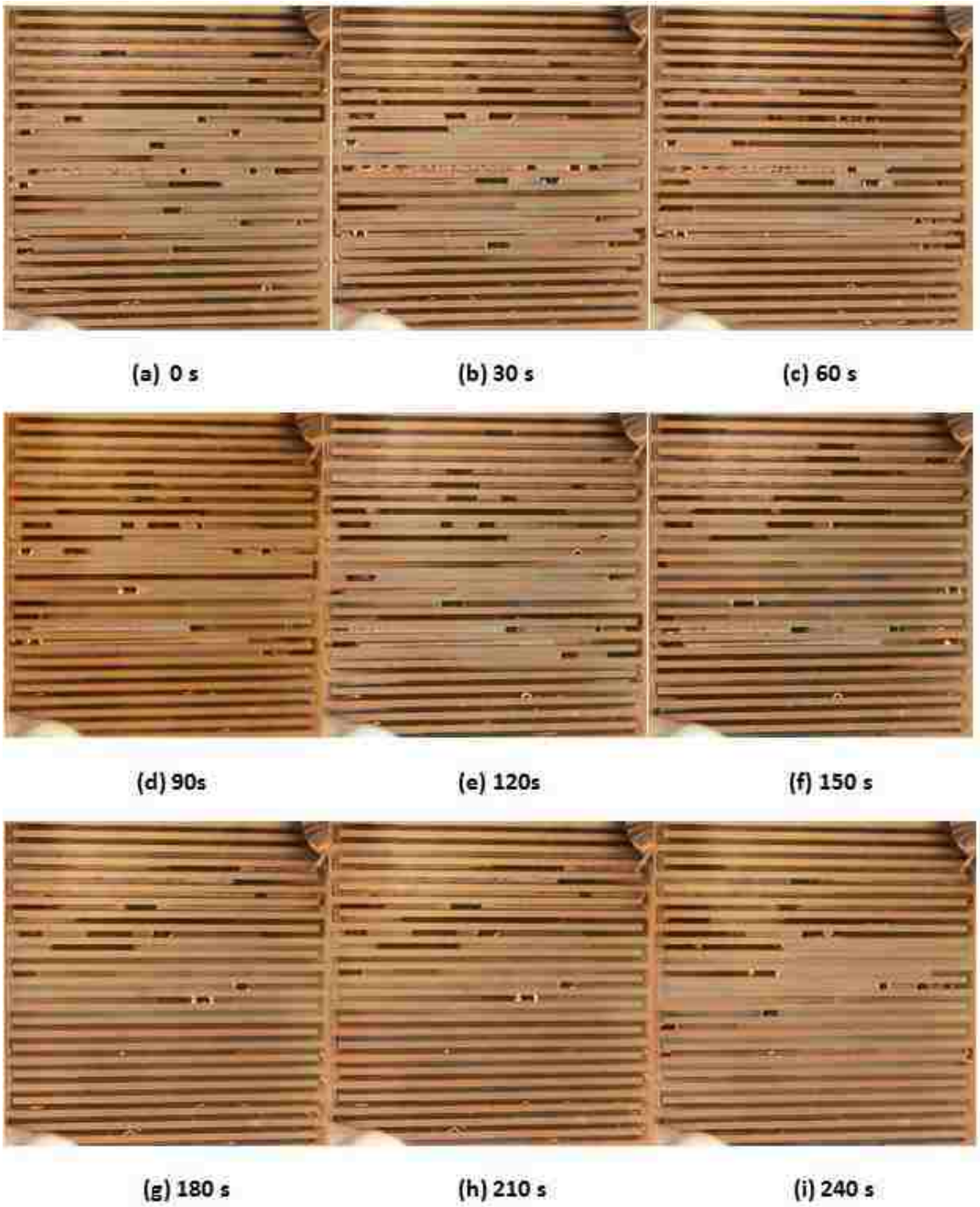

Figure 5.17 Time sequenced images showing water removal in single serpentine channels at 0.35 V

6 SUMMARY AND CONCLUSIONS

In this thesis, a proton exchange membrane (PEM) fuel cell with a bio-inspired bipolar plate design was experimentally and computationally evaluated for its water management capability and overall performance in comparison to a conventional single-serpentine flow field. The present bipolar plate design mimicked biological structures, such as leaf veins, in which branching channel dimensions followed the Murray's law for more uniform distribution of reactants.

In order to directly visualize the main product, liquid water, in the micro-channels, a transparent fuel cell assembly was designed and manufactured with copper as the conductive channel/current collector bonded to a clear Lexan plate. This special experimental setup was used to gain access to the inside of a bio-inspired fuel cell, possibly for the first time in the literature. The same transparent setup was also fabricated for a single-serpentine fuel cell so that the water management capability of the bio-inspired design could be compared with that of a conventional flow field. Liquid water transport and removal mechanisms of both PEM fuel cells were directly observed by digital photography at various operating conditions. The water dynamics were recorded at different times at three representative voltages while different types of flow regimes were also identified by inspecting the images of the two-phase flow in micro-channels.

Additionally, measurements of fuel cell voltages at different currents yielded the polarization and power density curves, which quantified the overall performances of both fuel cells. Finally, advanced computations were carried out based on a three-dimensional CFD model that provided predictions of pressure, velocity, reactant (hydrogen and oxygen) and product (water) distributions within the fuel cells. Such simulations were

compared to experimental results for a comprehensive understanding of water transport mechanisms and validating model predictions by identifying similarities and differences.

Overall, the visualization experiments reported in this study clearly demonstrated that the bio-inspired design managed the liquid water better compared to the traditional single-serpentine flow field. In particular, the optical images in the bio-inspired fuel cell showed that the plug formations were absent, reducing the pressure fluctuations within the inlet channels and therefore promoting more uniform reactant distributions. The interdigitated nature of the bio-inspired geometry also enhanced the water removal with under-rib flows in addition to the contribution from the compression on the GDL fibers. Some limited regions of inferior removal capabilities were also identified based on the observation that flows within the primary channels were sluggish. The digital photography and voltage measurements also indicated that, compared to the single-serpentine design, the water accumulation in the bio-inspired fuel cell was less with smaller voltage fluctuations at high currents where mass concentration losses dominated.

The detailed computations clearly established that the bio-inspired bipolar plate design distributed reactant concentrations and velocities more uniformly by enforcing higher reactant consumption rates. Additionally, the pressure differential between the inlet and outlet of the bio-inspired design enhanced mass transport through the GDL under the lands that facilitated quicker water removal. The simulations generally agreed well with the experiments at low and medium current densities, where the activation and ohmic losses were respectively more important. However, the differences between the computations and experiments gradually increased with the current density, reaching about 10-15% when the concentration losses dominated at the highest currents considered

here. This highlighted the shortcoming of the computational model, which could not completely capture the dynamics of the liquid water within the channels.

As a result of all the observations and explanations summarized above, the overall performance of the present bio-inspired design was superior compared to its conventional counterpart with the single serpentine flow field. Specifically, it produced higher voltages at relatively high current densities while providing a wider operational range by reducing the mass transport irreversibilities. Accordingly, the peak power density of the bio-inspired fuel cell was 30% higher compared to the single-serpentine geometry.

These complimentary experimental and computational results were crucial to elucidate the complex electrochemical processes and, therefore, significantly contributed to further improvement and optimization of nature-inspired PEM fuel cells. Finally, optimizing the flow fields to improve the distribution characteristics in tandem with finding better and cheaper membrane materials can help achieve the goals set forth by Department of Energy.

7 RECOMMENDED FUTURE WORK

The work presented above highlighted the water management capabilities of bio-inspired flow field designs. Although the results clearly demonstrated that the performance of this bio-inspired flow field design was superior mainly due to its better distribution of reactants and removal of water, they also indicated that there were some regions of inferior water management capabilities. In order to extend the present study, those regions need to be optimized to enhance the water handling capabilities. Additionally, focus must be on carefully designing optimizing the flow fields near the middle of the fuel cell where the water production rate was the highest. A possibility would be to design the channels at the middle for higher velocity ratios so as to enhance water removal. A multi-objective optimization scheme for optimizing pressure and velocity could be implemented because pressure and velocity are inversely proportional to each other and optimizing one parameter could affect the other adversely. Murray's law is an energy optimization scheme but does not focus on the individual contributions of pressure and velocity. Furthermore, active water management strategies could be investigated. Suggestively, with the help of Stereolithography (SLA), bipolar plates designed for active water management strategies with a network of miniature channels to alternatively remove water from the channels could be designed. But, the material limitations with this technology must be looked into. Lastly, the overall performance of a stack of bio-inspired fuel cells should be studied in order to extend the present results on a single design to practical applications.

BIBLIOGRAPHY

[1] Tsuchiya, H., Kobayashi, O. Mass production cost of PEM fuel cell by learning curve. International Journal of Hydrogen Energy, 2004, 29: 985-990.

[2] Kraytsberg, A., Auinat, M., Ein-Eli, Y. Reduced contact resistances of PEM fuel cell's bipolar plates via surface texturing. Journal of Power Sources, 2007, 164: 697-703.

[3] Makkus, P.C., Tanssen, A.H.H., de Bruijn, F.A. Mallant, R.K.A.M. Use of cost effective stainless steel for cost competitive bipolar plates in the SPFC. Journal of Power Sources, 2000, 86: 274-282.

[4] Oyarce, A., Holmstrom, N., Boden, A., Lagergren, C., Lindberg, G. Operating conditions affecting the contact resistance of bipolar plates in proton exchange membrane fuel cells. Journal of Power Sources, 2013, 231: 246-255.

[5] Avasarala, B., Haldar, P. Effect of surface roughness of composite bipolar plates on the contact resistance of a proton exchange membrane fuel cell. Journal of Power Sources, 2009, 188: 225-229.

[6] Guo, N., Leu, M.C. Effect of different graphite materials on the electrical conductivity and flexural strength of bipolar plates fabricated using selective laser sintering. International Journal of Hydrogen Energy, 2012, 34: 3558-3566.

[7] Manso, A.P., Marzo, F.F., Mujika, M.G., Barranco, J., Lorenzo, A. Numerical analysis of the influence of the channel cross-section aspect ratio on the performance of a PEM fuel cell with serpentine flow field design. International Journal of Hydrogen Energy, 2011, 36: 6795-6808.

[8] Wang, X., Lu, G., Duan, Y., Lee, D. Numerical analysis on performances of polymer electrolyte membrane fuel cells with various cathode flow channel geometries. International Journal of Hydrogen Energy, 2012, 37: 1-9.

[9] Tüber, K., Oedegaard, A., Hermann, M., Hebling, C. Investigation of fractal flow-fields in portable proton exchange membrane and direct methanol fuel cells. Journal of Power Sources, 2004, 131: 175-181.

[10] Friess, B.R., Hoorfar, M. Development of a novel radial cathode flow field for PEMFC. International Journal of Hydrogen Energy, 2012, 37: 7719-7729.

[11] Jang, J.-Y., Cheng, C.-H., Liao, W.-T., Huang, Y.-X., Tsai, Y.-C. Experimental and numerical study of proton exchange membrane fuel cell with spiral flow channels. Applied Energy, 2012, 99: 67-79.

[12] Roshandel, R., Arbabi, F., Moghaddam, K.G. Simulation of an innovative flow-field design based on a bio-inspired pattern for PEM fuel cells. Renewable Energy, 2012, 41: 86-95.

[13] Arvay, A., French, J., Wang, J.-C., Peng, X.-H., Kannan, A.M. Nature inspired flow field designs for proton exchange membrane fuel cell. International Journal of Hydrogen Energy, 2013, 38: 3717-3726.

[14] Kloess, J. P., Wang, X., Liu, J., Shi, Z., Guessous, L. Investigation of bio-inspired flow channel designs for bipolar plates in proton exchange membrane fuel cells. Journal of Power Sources, 2009, 188: 132-140.

[15] Sherman, T.F. On connecting large vessels to small: the meaning of Murray's law. The Journal of General Physiology, 1981, 78: 431-453.

[16] Li, H., Tang, Y., Wang, Z., Shi, Z., Wu, S., Song, D., Zhang, J., Fatih, K., Zhang, J., Wang, H., Liu, Z., Abouatallah, R., Mazz, A. A review of water flooding issues in the proton exchange membrane fuel cell. Journal of Power Sources, 2008, 178: 103-117.

[17] Anderson, R., Zhang, L., Ding, Y., Blanco, M., Bi, X., Wilkinson, D.P. A critical review of two-phase flow in gas flow channels of proton exchange membrane fuel cells. Journal of Power Sources, 2010, 195: 4531-4553.

[18] Hasan, A.B.M., Wahab, M.A., Guo, S.M. CFD analysis of a PEM fuel cell for liquid dispersion at the interface of GDL_GFC. International Journal of Numerical Methods for Heat & Fluid Flow, 2011, 21: 810-821.

[19] Djilali, N. Computational modelling of polymer electrolyte membrane (PEM) fuel cells: challenges and opportunities. Energy, 2007, 32: 269-280.

[20] Litster, S., Sinton, D., Djilali, N. Ex situ visualization of liquid water transport in PEM fuel cell gas diffusion layers. Journal of Power Sources, 2006, 154: 95–105.

[21] Lu, Z., Rath, C., Zhang, G., Kandlikar, S.G. Water management studies in PEM fuel cells, part IV: Effects of channel surface wettability, geometry and orientation on the two-phase flow in parallel gas channels. International Journal of Hydrogen Energy, 2011, 36: 9864-9875.

[22] Bazylak, A. Liquid water visualization in PEM fuel cells: a review. International Journal of Hydrogen Energy, 2009, 34: 3845-3857.

[23] Spernjak, D., Prasad, A.K., Advani, S.G. In situ comparison of water content and dynamics in parallel, single-serpentine, and interdigitated flow fields of polymer electrolyte membrane fuel cells. Journal of Power Sources, 2010, 195: 3553-3568.

[24] Lee, S.J., Lim, S.K., Park, G.-G., Kim, C.-S. X-ray imaging of water distribution in a polymer electrolyte fuel cell. Journal of Power Sources, 2008, 185: 867-870.

[25] Rosli, M.I., Borman, D.J., Ingham, D.B., Ismail, M.S., Ma, L., Pourkashanian, M. Transparent PEM fuel cells for direct visualization experiments. ASME Journal of Fuel Cell Science and Technology, 2010, 7: 061015 pp 1-7.

[26] Tüber, K., Pócza, D., Hebling, C. Visualization of water buildup in the cathode of a transparent PEM fuel cell. Journal of Power Sources, 2003, 124: 403-414.

[27] Spernjak, D, Prasad, A, Advani, S. Experimental investigation of liquid water formation and transport in a transparent single-serpentine PEM fuel cell. Journal of Power Sources 2007, 170: 334-344.

[28] Liu, X., Guo, H., Ma, C. Water flooding and two-phase flow in cathode channels of proton exchange membrane fuel cells. Journal of Power Sources, 2006, 156: 267-280.

[29] Guo, N., Leu, M.C. Performance investigation of polymer electrolyte membrane fuel cells using graphite composite plates fabricated by selective laser sintering. ASME Journal of Fuel cell Science and Technology, 2014, 11: 011003 pp 1-8.

[30] Guo, N., Leu, M.C., Koylu, U.O., Bio-inspired flow field designs for polymer electrolyte membrane fuel cells. International Journal of Hydrogen Energy, 2014, 39: 21185-21195.

[31] Jeon, D.H., Greenway, S., Shimpalee, S., Zee, J.W.V. The effect of serpentine flow-field designs on PEM fuel cell performance. International Journal of Hydrogen Energy, 2008, 33: 1052-1066.

[32] Oyarce, A., Holmström, N., Bóden, A., Lagergren, C., Lindberg, G. Operating conditions affecting the contact resistance of bi-polar plates in proton exchange membrane fuel cells. Journal of Power Sources, 2013, 231: 246-255.

[33] Liu, X., Guo, H., Ye, F., Ma, C.F. Flow dynamic characteristics in flow field of proton exchange membrane fuel cells. International Journal of Hydrogen Energy, 2008, 33: 1040-1057.

[34] Rezkallah, K.S. Weber number based flow-pattern maps for liquid gas flows at microgravity. Journal of Multiphase flow, 1996, 422(6): 1256-1270.

[35] Hussaini, I.S., Wang, C-Y. Visualization and quantification of cathode channel flooding in PEM fuel cells. Journal of Power Sources, 2009, 187: 444-451.

[36] Bezinger, J., Nehlsen, J., Blackwell, D., Brennan, T., Itescu, J. Water flow in the gas diffusion layer of PEM fuel cells. Journal of Membrane Science, 2005, 261: 9-106.

[37] Bazylak, A., Sinton, D., Liu, Z-S., Djilali, N. Effect of compression on liquid water transport and microstructure PEMFC gas diffusion layers. Journal of Power Sources, 2007, 163: 784-792.

[38] Painter, P.R., Eden, P., Bengtsson, H.U. Pulsatile blood flow, shear force, energy dissipation and Murray's Law. Theoretical biology and medical modelling. 2006, 3: 31 pp 1-10.

[39] Barber, R.W., Emerson, D.R., Biomimetic design of artificial micro-vasculatures for tissue engineering. ATLA (Alternative to Laboratory Animals), 2010, 38: 67-79.

[40] Fuel Cell Technologies Office Multi-Year Research, Development, and Demonstration (MYRD&D) Plan; Department of Energy, July, 2013, http://energy.gov/sites/prod/files/2014/03/f12/fuel_cells.pdf

[41] Li, W., Yu, A., Higgins, D. C., Llanos B. G. & Chen Z. Biologically inspired highly durable iron phthalocyanine catalysts for oxygen reduction reaction in polymer electrolyte membrane fuel cells. Journal of the American Chemical Society, 2010, 132: 17056–17058.

VITA

Venkatanaga Bhaskar Prakash Saripella was born in, Hyderabad, Andhra Pradesh, India. He received his B.E. in Mechanical Engineering from the Osmania University, Hyderabad, Andhra Pradesh, India in 2012. He graduated with distinction. He then began his graduate studies at the Missouri University of Science and Technology. He taught the Introduction to Engineering Design Laboratory course for four semesters. After successfully defending this thesis, he is expected to receive his M.S. degree in Mechanical Engineering from the Missouri University of Science and Technology, Rolla, Missouri, USA in May 2015. His research results are to be submitted to ASME Journal of Fuel Cell Science and Technology in January 2015 and presented at the ASME 13th Fuel Cell Science, Engineering, and Technology Conference in San Diego, CA, in June 2015.